

One pion production in neutrino reactions: Including nonresonant background

O. Lalakulich, T. Leitner, O. Buss, and U. Mosel

Institut für Theoretische Physik, Universität Giessen, Germany

(Received 16 July 2010; published 3 November 2010)

We investigate neutrino-induced one pion production on nucleons. The elementary neutrino-nucleon cross section is calculated as the sum of the leading Delta pole diagram and several background diagrams obtained within the nonlinear sigma model. This approach does not introduce any new adjustable parameters, which allows unambiguous predictions for the observables. Considering electroproduction experiments as benchmark, the model is shown to be applicable up to pion-nucleon invariant mass $W < 1.4$ GeV and provides a good accuracy. With respect to the total one pion cross section, the model predicts the background at the level of 10% for the $p\pi^+$, 30% for $p\pi^0$, and 50% for $n\pi^+$ final states. The results are compared with experimental data for various differential cross sections. Distributions with respect to muon-nucleon and muon-pion invariant masses are presented for the first time. The model describes the data quite well, with the discrepancies being of the same order as those between different data sets.

DOI: 10.1103/PhysRevD.82.093001

PACS numbers: 13.15.+g

I. INTRODUCTION

The interest in one pion production in neutrino-nucleus reactions has recently been revived in view of the current experimental search for neutrino oscillations. The neutrino energy spectra for the ongoing and coming long baseline neutrino experiments are typically peaked in the GeV region, the region where one pion production along with the quasielastic scattering gives a major contribution. Besides being interesting as a separate channel, pion production constitutes a noticeable background for various processes: the pion can be absorbed in the nucleus and thus mimic a quasielastic event; in Cherenkov detectors π^0 can mimic the outgoing electron. Thus, a precise knowledge of the corresponding cross sections is a prerequisite for the proper interpretation of the experimental data.

Understanding of one pion production includes two aspects: a proper description of the elementary process on nucleon and a proper treatment of the nuclear correction. Here we will concentrate on the elementary process.

In electromagnetic processes, the one pion production data, being plotted versus the invariant mass of the outgoing pion and nucleon, is seen as a series of peaks. This picture was a basis for the so-called isobar models, in which the intermediate state of the reaction was treated as a baryon resonance. The first prominent peak was shown to originate mainly from the Delta [$P_{33}(1232)$] excitation. The second broader peak receives contributions from the so-called second resonance region, which includes $P_{11}(1440)$, $D_{13}(1520)$, and $S_{11}(1535)$ resonances. In electroproduction the resonance excitations are known to be accompanied by the so-called nonresonant background, which can also interfere with the resonance contribution. Because the theoretical structure of the resonance contributions is known, the modern precise experiments on meson electroproduction allow the separation of these

contributions and the extraction of the information related to the resonances only; see, for example, [1] for a review. This information can be expressed in the form of the quasiexperimental “data points” for the invariant helicity amplitudes that characterize resonances and exclude background.

In neutrino production, the corresponding approach is, first, complicated by the fact that the cross section contains in addition to the vector current contribution also an axial one and a vector-axial interference contribution so that more resonance properties have to be determined. Second, any such extraction of such properties suffers from the absence of precise, high-statistics data. Here the data were obtained mainly in the 1980s in bubble chamber experiments. The most relevant ones are the hydrogen and deuterium data from the Argonne National Laboratory (ANL) and the Brookhaven National Laboratory (BNL) [2,3] which all suffer from low statistics (in comparison to the electroproduction data) so that only integrated and single-differential cross sections were reported. An additional experimental problem in these and all other neutrino experiments is that one cannot fix the neutrino energy, but has to deal with broad band neutrino beams. Thus, we are facing the problem of fixing both more complicated background and resonant parts from a very restricted set of data.

Within the phenomenological models, the way out of this situation was to presume that in the νp reaction, i.e. in the isospin-3/2 channel, there is no background for the Δ^{++} production (see, for example, [4–6]). This was motivated by, first, the measured πN invariant mass distribution in this channel and, second, by the absence of a nucleon Born term in this isospin-3/2 channel. Within this picture (once the vector form factors of the Δ production are considered to be fixed from electroproduction data), one can fit the Delta axial form factors and use them further for other channels. Recent progress in this direction was

achieved by refitting the vector form factors from the up-to-date electroproduction data on helicity amplitudes [7–9] and refitting the axial form factors in the combined analysis of the ANL and BNL experiments [10,11].

Even if the axial form factors are fitted to describe the data for the $p\pi^+$ final state, we have to go beyond the isobar concept and include background contributions when considering $p\pi^0$ and $n\pi^+$ final states. The simplest argument comes from the experimental observation that the cross sections for these two final states are approximately equal, while the Δ contribution alone gives $\sigma(p\pi^0)/\sigma(n\pi^+) = 2$. The calculated cross sections are also shown to be lower than the experimental data. Including higher resonances, in particular, the three isospin-1/2 states from the second resonance region, increases the cross sections and improves the situation somewhat, but does not account for the missing strength. The additional contributions required can be introduced within the assumption $\sigma(p\pi^0)/\sigma(n\pi^+) = 1/2$, (the so-called “isospin-1/2” background) [7]. A similar philosophy was applied recently in [9], where the vector part of the background was extracted from electroproduction, as it is described by the MAID group [12], and then the magnitude of the background was fitted to the ANL neutrino data.

The obvious way beyond this simplest picture is to treat the background as a sum of Feynman diagrams with a pion and a nucleon in the final state. Progress in this direction was achieved by Sato, Uno, and Lee [13], and recently by Hernandez, Nieves, and Valverde [14] and Barbero, López Castró and Mariano [15].

In this article we use the model presented in [14] and apply it to electron and neutrino scattering on nucleons. We consider various kinematic distributions and analyze their sensitivity to the background contributions. With the model at hand, we are also in the position to check the phenomenological treatment, used in the Giessen Boltzmann–Uehling–Uhlenbeck (GiBUU) transport model [16]. This model describes nucleon-, nucleus-, pion-, and electron-induced collisions from some hundred MeV up to hundreds of GeV within one unified framework. Recently, neutrino-induced interactions were also implemented for the energies up to few GeV with the results presented in [9,17–20]. The code is written in modular FORTRAN and is available for download as an open source [16].

All current neutrino-nucleon investigations concentrate on reproducing a limited number of distributions, which include inclusive cross section, Q^2 , and $W(N\pi)$ distribution [4–6,9,10,13,14,21,22]. At the same time, experimentally available data on distributions on the muon-pion and muon-nucleon invariant masses [2,3], which restrict the dynamics of any model even further, are ignored. We concentrate on interactions with nucleon targets and aim at reproducing those distributions. Interactions with nuclei will be discussed in a forthcoming publication and are not considered in this work.

The article is organized as follows. First, we give a short description of the model used. Then we discuss the electron interactions in the Delta resonance region, producing $p\pi^0$ and $n\pi^+$ final states. We especially consider the resonance-background interference and possibility to introduce a simplified description of the background similar to the one discussed earlier [9]. Afterward, results for neutrino interactions are presented and compared with the available experimental data.

II. SHORT DESCRIPTION OF THE MODEL

In this section we give details about the model we use for the lepton-nucleon interactions. We are studying the process of one pion production in lepton interactions with nucleons, i.e.

$$l(k_\mu)N(p_\mu) \rightarrow l(k'_\mu)N(p'_\mu)\pi(p_\mu)$$

for various isospin final states.

The 5-fold cross section for one pion production is given by

$$\begin{aligned} & \frac{d\sigma}{dE' d\cos\theta dE_\pi d\cos\theta_\pi d\phi_\pi} \\ &= \frac{|M^2|}{4\sqrt{(pk)^2 - m_N^2 m_l^2}} \frac{1}{(2\pi)^4} \\ & \times \frac{|\vec{k}'||\vec{p}_\pi|}{8E'_p} \cdot \delta(E + E_p - E' - E_\pi - E'_p). \quad (1) \end{aligned}$$

The dynamics of the interaction is encoded in the matrix elements for electromagnetic (EM) and charged current (CC) interactions

$$|M^2| = C_{\text{EM,CC}} L^{\mu\nu} H_{\mu\nu}, \quad H_{\mu\nu} = j_\mu j_\nu^\dagger,$$

where

$$C_{\text{EM}} = \frac{4\pi\alpha_{\text{QED}}}{Q^2}, \quad C_{\text{CC}} = \frac{G_F}{2} \cos\theta.$$

The calculation of the leptonic tensor $L^{\mu\nu}$ is straightforward and gives the standard result. The hadronic tensor $H_{\mu\nu}$ reflects the essence of the process taken into account. The hadronic current j_ν varies from model to model and can include various contributions.

Several authors have proposed to describe the current as a coherent sum of several diagrams [13,14,23]: Delta pole (Dp), crossed Delta pole (cDp), nucleon pole (Np), crossed nucleon pole (cNp), contact term (CT), pion pole (pp), and pion in flight (pF),

$$j = j_{\text{Dp}} + j_{\text{cDp}} + j_{\text{Np}} + j_{\text{cNp}} + j_{\text{CT}} + j_{\text{pp}} + j_{\text{pF}}.$$

The diagrams considered are shown in Fig. 1.

The progress in understanding the background can, however, be only achieved, if the new vertices introduced

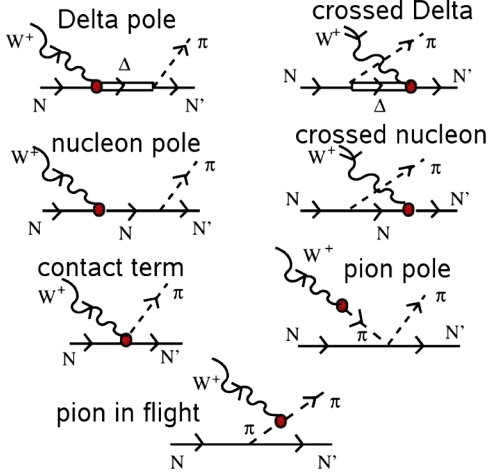


FIG. 1 (color online). Diagrams representing the Δ pole and background contributions to the one pion production in weak charged current scattering on the nucleon [14].

are considered as known and do not include adjustable parameters.

Hernandez *et al.* [14] (from now on called the HNV model) have proposed to use the vertices predicted by an effective Lagrangian of the $SU(2)$ nonlinear σ model.

The details of the model and the amplitudes of the diagrams are given in [14], and we repeat them here only for convenience:

$$j_{\text{Dp}}^{\mu} = iC^{\text{Dp}} \frac{f^*}{m_{\pi}} \cos\theta_C \frac{p_{\pi}^{\alpha}}{p_{\Delta}^2 - M_{\Delta}^2 + iM_{\Delta}\Gamma_{\Delta}} \times \bar{u}(\vec{p}') S_{\alpha\beta}(p+q) \Gamma_{3/2+}^{\beta\mu}(p, q) u(\vec{p}), \quad (2)$$

$$j_{\text{cDp}}^{\mu} = iC^{\text{cDp}} \frac{f^*}{m_{\pi}} \cos\theta_C \frac{p_{\pi}^{\beta}}{p_{\Delta}^2 - M_{\Delta}^2 + iM_{\Delta}\Gamma_{\Delta}} \times \bar{u}(\vec{p}') \gamma^0 [\Gamma_{3/2+}^{\alpha\mu}(p', -q)]^{\dagger} \gamma^0 S_{\alpha\beta}(p' - q) u(\vec{p}), \quad (3)$$

$$j_{\text{Np}}^{\mu} = -iC^{\text{Np}} \frac{g_A}{2f_{\pi}} \cos\theta_C \bar{u}(\vec{p}') \not{p}_{\pi} \gamma_5 \frac{\not{p} + \not{q} + M_N}{(p+q)^2 - M_N^2 + i\epsilon} \times [V_N^{\mu} - A_N^{\mu}] u(\vec{p}), \quad (4)$$

$$j_{\text{cNp}}^{\mu} = -iC^{\text{cNp}} \frac{g_A}{2f_{\pi}} \cos\theta_C \bar{u}(\vec{p}') [V_N^{\mu} - A_N^{\mu}] \times \frac{\not{p}' - \not{q} + M_N}{(p' - q)^2 - M_N^2 + i\epsilon} \not{k}_{\pi} \gamma_5 u(\vec{p}), \quad (5)$$

$$j_{\text{CT}}^{\mu} = -iC^{\text{CT}} \frac{1}{\sqrt{2}f_{\pi}} \cos\theta_C \bar{u}(\vec{p}') \gamma^{\mu} (g_A F_{\text{CT}}^V(Q^2) \gamma_5 - F_{\rho}((q - p_{\pi})^2)) u(\vec{p}), \quad (6)$$

$$j_{\text{pp}}^{\mu} = -iC^{\text{pp}} F_{\rho}((q - p_{\pi})^2) \frac{1}{\sqrt{2}f_{\pi}} \cos\theta_C \bar{u}(\vec{p}') \not{q} u(\vec{p}), \quad (7)$$

$$j_{\text{pF}}^{\mu} = -iC^{\text{pF}} F_{\text{pF}}(Q^2) \frac{g_A}{\sqrt{2}f_{\pi}} \cos\theta_C \times \frac{(2p_{\pi} - q)^{\mu}}{(p_{\pi} - q)^2 - m_{\pi}^2} 2M_N \bar{u}(\vec{p}') \gamma_5 u(\vec{p}). \quad (8)$$

Here $g_A = 1.26$ is the axial nucleon coupling and $f_{\pi} = 0.093$ GeV is the pion weak decay constant, which enter the Lagrangian of the σ model. The currents defined in (2)–(8) can be used for electromagnetic and weak processes, provided that the corresponding form factors and isospin coefficients $C^{\text{Dp, cDp, Np, cNp, CT, pp, pF}}$ are given. In the following we summarize them.

A. Delta resonance

In the HNV model the vertices of Δ production and decay (which enter the Delta pole and crossed Delta pole diagrams) are treated on the same theoretical grounds as earlier in [6,21,22].

The Δ production vertex, $\Gamma^{\beta\mu}$, is described as a vertex for the isospin-3/2 resonance production

$$\Gamma_{3/2+}^{\beta\mu} = [\mathcal{V}_{3/2}^{\beta\mu} - \mathcal{A}_{3/2}^{\beta\mu}] \gamma_5. \quad (9)$$

and used in Eqs. (2) and (3). In terms of the phenomenological form factors, the vector part is given by

$$\mathcal{V}_{3/2}^{\beta\mu} = \frac{C_3^V}{m_N} (g^{\beta\mu} \not{q} - q^{\beta} \gamma^{\mu}) + \frac{C_4^V}{m_N^2} (g^{\beta\mu} q \cdot p' - q^{\beta} p'^{\mu}) + \frac{C_5^V}{m_N^2} (g^{\beta\mu} q \cdot p - q^{\beta} p^{\mu}), \quad (10)$$

and the axial part by

$$-\mathcal{A}_{3/2}^{\beta\mu} = \left[\frac{C_3^A}{m_N} (g^{\beta\mu} \not{q} - q^{\beta} \gamma^{\mu}) + \frac{C_4^A}{m_N^2} (g^{\beta\mu} q \cdot p' - q^{\beta} p'^{\mu}) + C_5^A g^{\beta\mu} + \frac{C_6^A}{m_N^2} q^{\beta} q^{\mu} \right] \gamma_5. \quad (11)$$

The calligraphic C_i^V stands either for the electromagnetic transition form factors C_i^N with $N = p, n$ or the CC vector form factors C_i^V . For the Δ resonance, they coincide and—in line with [14]—we use the fit of [7]:

$$C_3^V(Q^2) = C_3^{(p,n)}(Q^2) = \frac{2.13}{D_V(Q^2)} \cdot \frac{1}{1 + Q^2/4M_V^2},$$

$$C_4^V(Q^2) = C_4^{(p,n)}(Q^2) = \frac{-1.51}{D_V(Q^2)} \cdot \frac{1}{1 + Q^2/4M_V^2},$$

$$C_5^V(Q^2) = C_5^{(p,n)}(Q^2) = \frac{0.48}{D_V(Q^2)} \cdot \frac{1}{1 + Q^2/0.776M_V^2}.$$

The function $D_V(Q^2) = (1 + Q^2/M_V^2)^2$ denotes the dipole function with the vector mass parameter $M_V = 0.84$ GeV. (The axial form factors are relevant only for CC interactions.) Notice, that in general, the currents for different isospin channels differ from one another by Clebsch-Gordon coefficients. In the present work these are included

in Eqs. (2)–(8) and defined in Table I. Thus, the form factors are the same for different final states.

The axial form factors are taken to be the same as in [14], where $C_5^A(Q^2)$ was fitted to the ANL cross section:

$$C_5^A(Q^2) = \frac{0.867}{D_A(Q^2)} \cdot \frac{1}{1 + Q^2/3M_A^2},$$

$$C_4^A(Q^2) = -\frac{1}{4}C_5^A(Q^2), \quad C_3^A(Q^2) = 0, \quad C_6^A(Q^2) = 0,$$

with $D_A(Q^2) = (1 + Q^2/M_A^2)^2$ and $M_A = 0.985$ GeV.

The value $C_5^A(0) = 0.867$ obtained in [14] is in contradiction with the predictions of the off-diagonal Goldberger-Treiman relation, which expresses $C_5^A(0)$ via the $\Delta N\pi$ coupling constant f^* and gives the value 1.2. This relation is based on the partial conservation of axial current (PCAC) hypothesis, which was tested in several experiments and is shown to be satisfied with an accuracy not worse than 10% [24–26]. When considering both ANL and BNL data, the recent fit [11] gives $C_5^A(0) = 1$, which is closer to the PCAC prediction, but still is outside the 10% deviation from it. In [9] the ANL data were described with a fit for C_5^A , that fulfills PCAC.

The spin-3/2 projector is taken in conventional Rarita-Schwinger form

$$S_{\alpha\beta}(p_\Delta) = -(p^\Delta + M_\Delta) \left(g_{\alpha\beta} - \frac{2}{3} \frac{p_\alpha^\Delta p_\beta^\Delta}{M_\Delta^2} + \frac{1}{3} \frac{p_\alpha^\Delta \gamma_\beta - p_\beta^\Delta \gamma_\alpha}{M_\Delta} - \frac{1}{3} \gamma_\alpha \gamma_\beta \right)$$

and used in Eqs. (2) and (3).

The coupling f^* of the $\Delta N\pi$ vertex in j_{Dp} and j_{cDp} currents is determined from the free decay width of the Δ resonance, $f^* = 1.15$ [14].

TABLE I. Clebsch-Gordan coefficients for various final states in EM and CC interactions.

	$p\pi^+$	$p\pi^0$	$p\pi^-$	$n\pi^+$	$n\pi^0$	$n\pi^-$
EM						
Dp	0	$\sqrt{2/3}$	$\sqrt{1/3}$	$-\sqrt{1/3}$	$\sqrt{2/3}$	0
cDP	0	$\sqrt{2/3}$	$-\sqrt{1/3}$	$\sqrt{1/3}$	$\sqrt{2/3}$	0
Np	0	$\sqrt{1/2}$	1	1	$-\sqrt{1/2}$	0
cNp	0	$\sqrt{1/2}$	1	1	$-\sqrt{1/2}$	0
CT, pF	0	0	1	-1	0	0
pp	0	0	0	0	0	0
CC						
Dp	$\sqrt{3}$	$-\sqrt{2/3}$	$\sqrt{1/3}$	$\sqrt{1/3}$	$\sqrt{2/3}$	$\sqrt{3}$
cDP	$\sqrt{1/3}$	$\sqrt{2/3}$	$\sqrt{3}$	$\sqrt{3}$	$-\sqrt{2/3}$	$\sqrt{1/3}$
Np	0	$\sqrt{1/2}$	1	1	$-\sqrt{1/2}$	0
cNP	1	$-\sqrt{1/2}$	0	0	$\sqrt{1/2}$	1
CT, pp, pF	1	$-\sqrt{2}$	-1	-1	$\sqrt{2}$	1

B. Nucleon

The vertices with nucleons and pions are described within the $SU(2)$ nonlinear σ model. Within this model all the vertices are pointlike, including the coupling VNN of a nucleon to the vector or axial current.

The authors of [14] choose to introduce nucleon form factors to the VNN vertex in a phenomenological way. All these form factors are considered to be known and can be taken from one of the conventional parametrizations.

For the nucleon vertex, we adopt the standard hadronic current $\mathcal{V}_N^\mu - \mathcal{A}_N^\mu$

$$\mathcal{V}_N^\mu = \mathcal{F}_1 \gamma^\mu + i \frac{\mathcal{F}_2}{2M_N} \sigma^{\mu\alpha} q_\alpha, \quad (12)$$

and the axial part

$$-\mathcal{A}_N^\mu = F_A \gamma^\mu \gamma_5 + \frac{F_P}{M_N} q^\mu \gamma_5. \quad (13)$$

Here, \mathcal{F}_i^V ($i = 1, 2$) stands either for the EM nucleon form factors F_i^N with $N = p, n$ or the CC form factors $F_i^V = F_i^p - F_i^n$. The electromagnetic Dirac and Pauli form factors F_i^N can be rewritten in terms of Sachs form factors, for which we take the updated BBBA-2007 parametrization [27]. The axial form factors are relevant only for CC reactions and for them we assume a standard dipole form with the axial mass determined in [28]:

$$F_A(Q^2) = g_A \left(1 + \frac{Q^2}{M_A^2} \right)^{-2}, \quad M_A = 0.999 \text{ GeV},$$

$$F_P(Q^2) = \frac{2m_N^2}{Q^2 + m_\pi^2} F_A(Q^2). \quad (14)$$

C. Other diagrams

As soon as nucleon form factors are introduced in the model, the conservation of the vector current

$$q^\mu (j_{Dp} + j_{cDp} + j_{Np} + j_{cNp} + j_{CT} + j_{pp} + j_{pF})_\mu \stackrel{!}{=} 0 \quad (15)$$

is no longer fulfilled. The way to compensate in Eq. (15) the nonvanishing terms stemming from j_{Np} and j_{cNp} is to introduce the corresponding form factors to j_{CT} and j_{pF} . As outlined in [14], for charged current processes, the corresponding form factors are the same as the weak vector nucleon ones. It can be shown, that for electroproduction processes, they also stay the same, i.e.,

$$F_{CT}^{\text{em}}(Q^2) = F_{CT}^{\text{CC}}(Q^2) = F_1^p(Q^2) - F_1^n(Q^2),$$

$$F_{pF}^{\text{em}}(Q^2) = F_{pF}^{\text{CC}}(Q^2) = F_1^p(Q^2) - F_1^n(Q^2). \quad (16)$$

Another phenomenological factor, introduced in the HNV model, is F_ρ , which accounts for the ρ -meson dominance in the axial parts of the CT and pp currents.

For CC reactions F_ρ is given by

$$F_\rho^{CC}(Q^2) = \frac{1}{1 + Q^2/m_\rho^2}, \quad m_\rho = 0.77 \text{ GeV},$$

and for EM interactions it is zero,

$$F_\rho^{\text{em}}(Q^2) = 0.$$

To summarize, the HNV model [14] phenomenologically extends the “pure” nonlinear $SU(2)$ model, but introduces no adjustable parameters. Besides the nucleon and the pion, the model contains only the Delta resonance and thus is applicable to the region below and slightly above the Delta peak.

III. ELECTROPRODUCTION AS BENCHMARK FOR NEUTRINO PRODUCTION

In this section, we present the differential cross section results for electron scattering, with the purpose to check the accuracy of the model and the range of its applicability.

We consider electrons of energy $E_e = 1.884 \text{ GeV}$ scattered on protons over the angle $\theta = 47.94^\circ$ ($\cos\theta = 0.67$) and calculate the double differential cross section $d\sigma/d\Omega_e dE_e$.

Figure 2(a) shows the full model cross section (solid line), obtained as a coherent sum of all the diagrams. It is compared with JLab electroproduction data [29]. Notice, that these data are for the inclusive cross section, while our curve is for the one pion production, that is for the sum of the $p\pi^0$ and $n\pi^+$ final states, only. Below and at the Δ peak, our calculations agree perfectly with the data. At the same time, the Delta pole diagram alone (dash-dotted line) is noticeably below the data. Above the Δ peak, as expected, the data lie above our curve, because other resonances contribute in this region as well as other channels (for example, two pion production and eta production) become kinematically allowed. The incoherent sum of all the diagrams (short-dashed line) is also shown in Fig. 2. Below the Δ peak the interference effects are small, while above the Delta peak the interference is strong and negative.

The similar picture is also shown in Fig. 2(b) for $E_e = 2.238 \text{ GeV}$ and $\theta = 31.93^\circ$ ($\cos\theta = 0.8487$). The agreement with the data is again very good below and at the Δ peak.

Conventionally, experimental results for one pion production are shown in the form of the cross section for virtual photons

$$\frac{1}{\Gamma_\gamma} \frac{d\sigma}{d\Omega' dE'} = \sigma_T + \varepsilon\sigma_L, \quad (17)$$

where Γ_γ is the flux of the virtual photon field

$$\Gamma_\gamma = \frac{\alpha_{\text{QED}}}{2\pi^2} \frac{E'}{E_e} \frac{W^2 - m_N^2}{2m_N Q^2} \frac{1}{1 - \varepsilon},$$

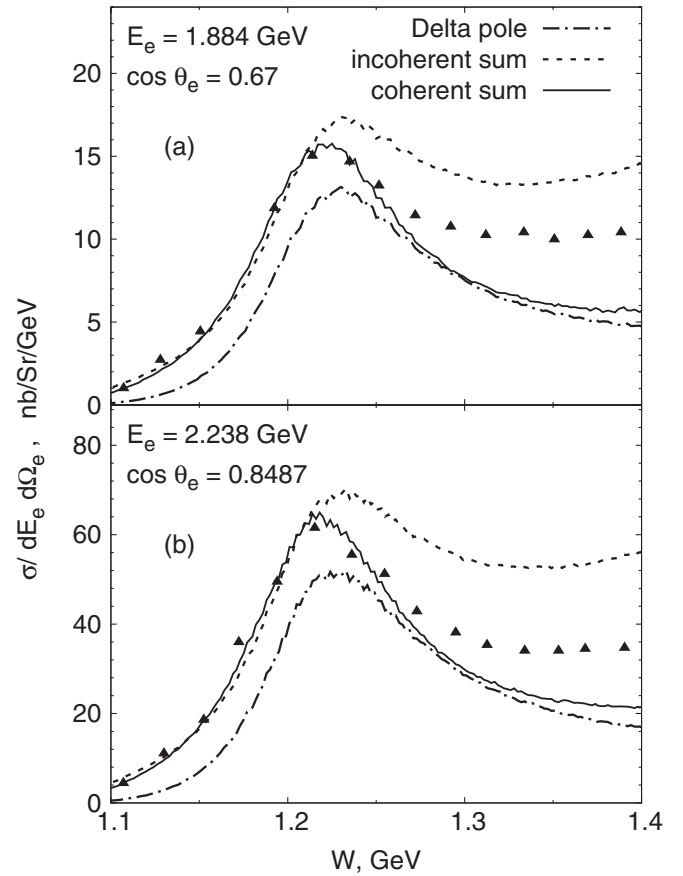


FIG. 2. Differential cross section for $ep \rightarrow e\Delta^+$ at $E_e = 1.884 \text{ GeV}$, $\theta_e = 47.94^\circ$ (a) and at $E_e = 2.238 \text{ GeV}$, $\theta_e = 31.93^\circ$ compared to the inclusive $ep \rightarrow eX$ data [29].

and ε is the degree of transverse polarization of the photon

$$\varepsilon = \left[1 + 2 \left(1 + \frac{\nu^2}{Q^2} \right) \tan^2 \frac{\theta}{2} \right]^{-1}.$$

Here θ is the electron scattering angle, ν the energy transfer, Q^2 the squared momentum transfer, and $W^2 = m_N^2 + 2m_N\nu - Q^2$ the invariant mass of the final nucleon-pion state.

Our results are compared to the DESY electron-proton scattering data [30] in Fig. 3 for $p\pi^0$ and $n\pi^+$ final states (middle and lower panels). Two data sets are available: (1) for electron energy $E_e = 2.7 \text{ GeV}$ and the scattering angle of 14° , at the Δ peak position $Q^2 = 0.35 \text{ GeV}^2$; and (2) for electron energy $E_e = 3.2 \text{ GeV}$ and the scattering angle of 21° , at the Δ peak position $Q^2 = 1.0 \text{ GeV}^2$. The figure shows the cross section (17) versus the outgoing electron energy E' in the Δ region. Here the higher E' values corresponds to lower invariant masses W . We present the full model calculations (solid lines), as well as the contribution of the Delta pole alone (dashed lines).

The predictions of the MAID model [12,31] are also shown as crosses, which provides us an overall comparison

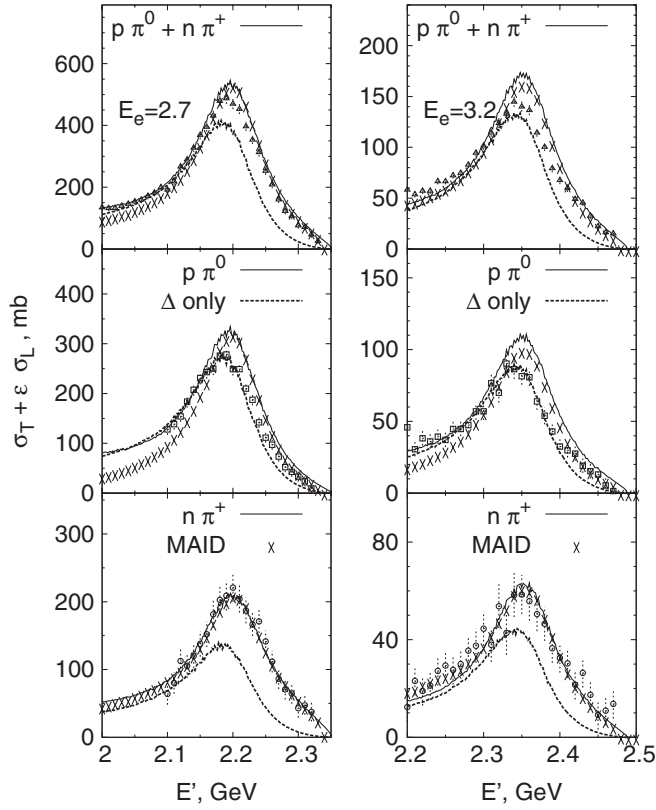


FIG. 3. Cross section (17) for $ep \rightarrow ep\pi^0$ (middle panel) and $ep \rightarrow en\pi^+$ (lower panel) at $E_e = 2.7$ GeV, $\theta_e = 14^\circ$ (left panel) and $E_e = 3.2$ GeV, $\theta_e = 21^\circ$ (right panel) as a function of outgoing electron energy E' compared to the data [30]. The predictions of the MAID model are shown as crosses.

with modern electroproduction data. The MAID model, developed by Mainz theory group, is a state-of-the-art unitary isobar model for pion photo and electroproduction on the nucleon, which fits more than 70000 data points on 5 and more fold differential cross sections. For the GiBUU code, it provides the resonance amplitudes for electroproduction. The results of the MAID model for double differential cross section can be considered as being equivalent to the data. They can, therefore, serve as a benchmark for our calculation that—contrary to MAID—contains a theoretically well founded description of the background amplitudes.

The full model calculations show an excellent agreement with the data [30] for the $n\pi^+$ final state. At high E' , corresponding to the invariant mass region below the Delta resonance, we observe a noticeable increase of the cross section in comparison with the Delta pole diagram, which significantly improves the agreement with the data. With decreasing E' , the invariant mass W increases, reaching $W = 1.29$ GeV at the left end of the data points for $E_e = 2.7$ GeV and $W = 1.35$ GeV for $E_e = 3.2$ GeV. For the $p\pi^0$ final state, our full model, as well as the MAID model, shows a reasonable agreement with the data.

The data are also available for the sum of the final states $p\pi^0 + n\pi^+$ (triangles in the upper panel of Fig. 3), they agree with our curves up to $W = 1.4$ GeV. In all cases the full model calculations are very close to the MAID results. Thus, the model provides the same level of accuracy as the MAID model, which ensures the applicability of the HNV model to the leptonproduction processes at least up to $W < 1.4$ GeV.

IV. NEUTRINO PRODUCTION

In this section we present our results for neutrinos.

The double differential cross sections $d\sigma/dE_\mu d\cos\theta_\mu$ for the charged current neutrino reactions versus the nucleon-pion invariant mass W are presented in Fig. 4 for the incoming neutrino energy $E_\nu = 1$ GeV and the muon scattering angle $\cos\theta_\mu = 0.6$. As we already mentioned, the form factors used are taken to be same as in [14], in particular we use the same C_5^A . Figure 4(a) shows the contribution of each diagram to the cross section for the $p\pi^+$ final state. For this channel, the cross sections

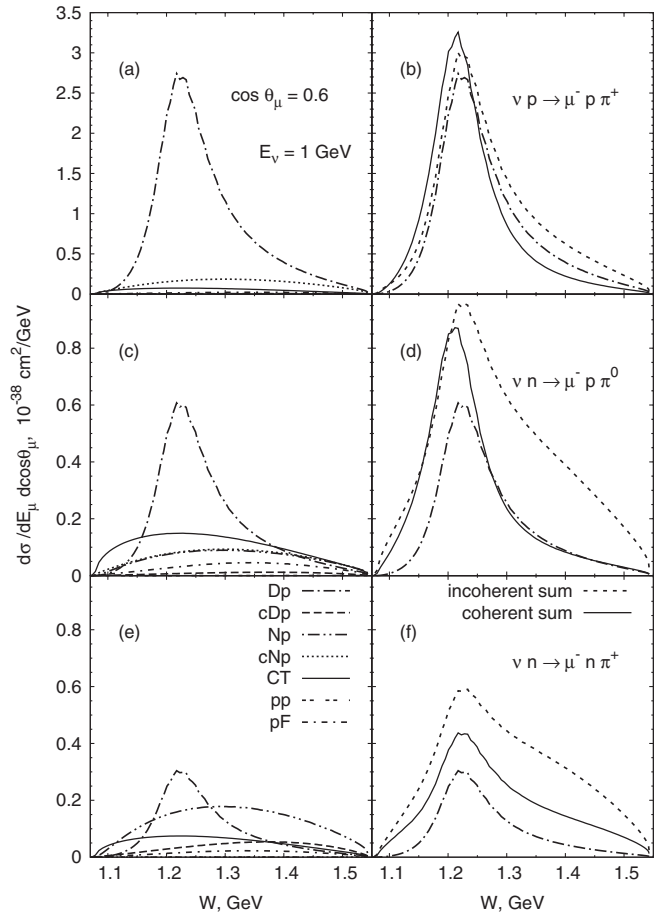


FIG. 4. Double differential cross section $d\sigma/dE_\mu d\cos\theta_\mu$ for various final states for $E_\nu = 1$ GeV, $\cos\theta = 0.6$. Contributions of each diagram (a, c, e), as well as their coherent and incoherent sums (b, d, f) are shown.

for the background diagrams are indeed small in comparison with the Delta pole contribution. Figure 4(b) compares the full model calculation (solid line) with the Delta pole only (dash-dotted line) and with the incoherent sum (short-dashed line) of all diagrams. For the kinematics considered, the interference effect is negative above the Δ peak, and positive below the Δ peak.

Figures 4(c)–4(f) show the same cross section for a neutron target for the two possible final states, $p\pi^0$ and $n\pi^+$. As one can see, the background terms are noticeable in these cases. The most important contribution is given by the CT diagram, which provides a rather steep rise of the cross section at low W . The Np diagram dominates the background for the $n\pi^+$ channel and, together with the cDp, gives a large contribution for the $p\pi^0$ one. The way the background appears in reactions with a neutron target can partly be traced to pure isospin relations. For example, as can easily be deduced from Table I, the leading isobar contribution, Dp, for the $n\pi^+$ channel is 9 times smaller than that for the $p\pi^+$ one. At the same time, the cDp term, which was very small for the $p\pi^+$, is 9 times bigger for the $n\pi^+$ and thus becomes noticeable. From Figs. 4(d) and 4(f) one can see, that the interferences are again negative above the Δ peak, and small (positive or negative) below the Δ peak. The overall increase of the cross section in comparison with the Delta pole contribution is, as expected, much more significant than for the proton target.

A feature of the HNV model is that it introduces the background not only for the $p\pi^0$ and $n\pi^+$ final states, but also for the $p\pi^+$, that is for the isospin-3/2 channel. We observe, that in this channel the contribution of the background is at the level of 10%, which agrees with the result of [14]. This justifies the neglect of the background in the isospin-3/2 channel as assumed in earlier works [7,9,10,21,32] and explains why they were still successful in describing the data.

V. GENERAL FEATURES OF EFFECTIVE BACKGROUND

As the next step, in Fig. 5 we present our results for the integrated cross section, with the kinematical cut for the nucleon-pion invariant mass $W(N\pi) < 1.4$ GeV, versus the neutrino energy. The calculations are made for various final states and compared with data and with some previous theoretical results.

The simplest channel to compare with is the scattering on a proton target, because only one final state, $p\pi^+$, is possible. The full model calculation (solid line) appears to be slightly above the Delta pole contribution (dash-dotted line) and coincides with the previous calculation [9] (dashed line labeled “Leitner 09”) at small neutrino energies.¹ With increasing E_ν , the Leitner 09 curve, as

¹This implementation is available in the current open-source version of GiBUU [16].

expected, increases more steeply than the full model curve because the calculation [9] was done without any kinematical cut, while our calculation implies $W(N\pi) < 1.4$ GeV. Comparison with Fig. 5 in [14] shows, as expected, that the integrated cross sections is also very close to the original HNV result.

For the reactions on the neutron two final states, $n\pi^+$ and $p\pi^0$, are possible. For both of them, the full model cross sections are close to the previous GiBUU results [9], but have slightly different shapes. Keep in mind, that the W cuts are different.²

The ANL data can be described quite well for all channels and over the full energy range. This agreement is trivial for the $p\pi^+$ channel because, as we mentioned before, the axial form factors were fitted to them. The agreement for the two other channel shows that the model gives a very reasonable estimate for the integrated background.

A few data points from the Gargamelle propane experiment at CERN PS [33] are also available for antineutrino reactions on neutron $\bar{\nu}n$ and nucleon $\bar{\nu}N$, the latter being the sum over proton and neutron targets. Our full model calculations for the three possible final states, $\bar{\nu}n \rightarrow \mu^+ n\pi^-$, $\bar{\nu}p \rightarrow \mu^+ n\pi^0$, and $\bar{\nu}p \rightarrow \mu^+ p\pi^-$, are shown in Fig. 6 and compared to the Gargamelle experiment. The data on the $p\pi^-$ channel are obtained as

$$\begin{aligned} \sigma(\bar{\nu}p \rightarrow \mu^+ p\pi^-) \\ = \sigma(\bar{\nu}N \rightarrow \mu^+ N\pi^-) - \sigma(\bar{\nu}n \rightarrow \mu^+ n\pi^-). \end{aligned}$$

The results of our calculations are very close to those presented in the HNV paper [14]. The cross section for $n\pi^-$ is overestimated, while that for $p\pi^-$ shows a good agreement with the data.

Comparing the curves for the full model and Delta pole contributions, one can define the effective background by subtraction:

$$\sigma^{\text{eff-bgr}} = \sigma^{\text{full model}} - \sigma^{\text{Delta pole}}.$$

By definition, $\sigma^{\text{eff-bgr}}$ includes interference terms and thus can take positive or negative values. This effective background can be compared with the phenomenological background used in [9].

²For the $p\pi^0$ channel, our result is also in agreement with the original HNV calculation [14] (see Fig. 5 there), while for the $n\pi^+$ channel it is noticeably higher (at $E_\nu = 1.6$ GeV our result 0.12×10^{-38} cm² versus HNV 0.08×10^{-38} cm²). To understand this difference, we compared our calculations for each diagram with the corresponding unpublished results of the HNV group. We found a very good agreement for all diagrams except cDp, which in our calculations appears to be around 1.7 times smaller. Comparing the Clebsch-Gordon coefficients for various final states (see Table I) among themselves, one can notice that the cDp diagram contributes mainly to the $n\pi^+$ channel. Taking into account possible interferences, we attribute the difference in this channel to this contribution.

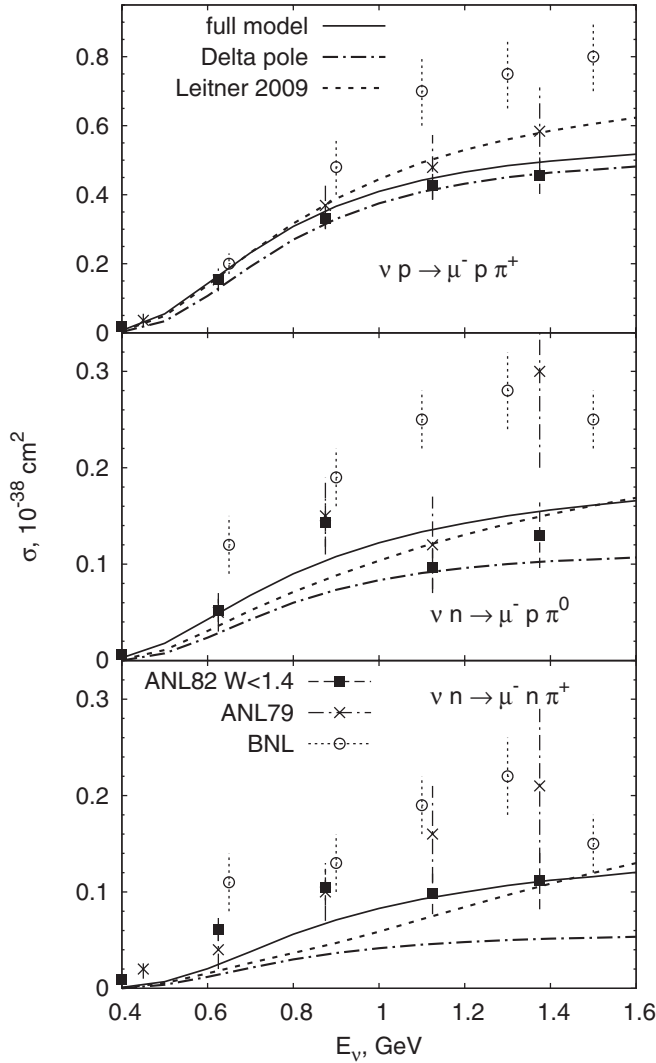


FIG. 5. The integrated one pion cross section, with kinematical cut $W(N\pi) < 1.4$ GeV versus neutrino energy for various final states. The full model calculations (solid line) are compared with the Delta pole contribution (dash-dotted line) and previous calculations of Leitner *et al* [9] (dashed line).

Figure 7 shows the effective background for the three final states. For the $p\pi^+$ final state (long-dashed line), it is at the level of $0.04 \times 10^{-38} \text{ cm}^2$ for all values of E_ν . For a neutron target the background is growing with energy taking on about the same values for the $p\pi^0$ (solid line) and $n\pi^+$ (short-dashed line) final states.

In earlier phenomenological approaches [7,9], the assumption of the isospin-1/2 background was used, which presupposes $\sigma_{\text{bgr}-1/2}^{n\pi^+} = 2\sigma_{\text{bgr}-1/2}^{p\pi^0}$; this curve is shown as a dash-dotted line. Thus, one can conclude, that the effective background does not follow the isospin-1/2 approximation. Indeed, from the six diagrams (cDp, Np, cNp, CT, pp, pF) directly contributing to the background, only one (Np) satisfies the isospin-1/2 hypothesis, that is, its Clebsch-Gordon coefficients are related as $C_{n\pi^+}^{\text{Np}} = \sqrt{2}C_{p\pi^0}^{\text{Np}}$. For

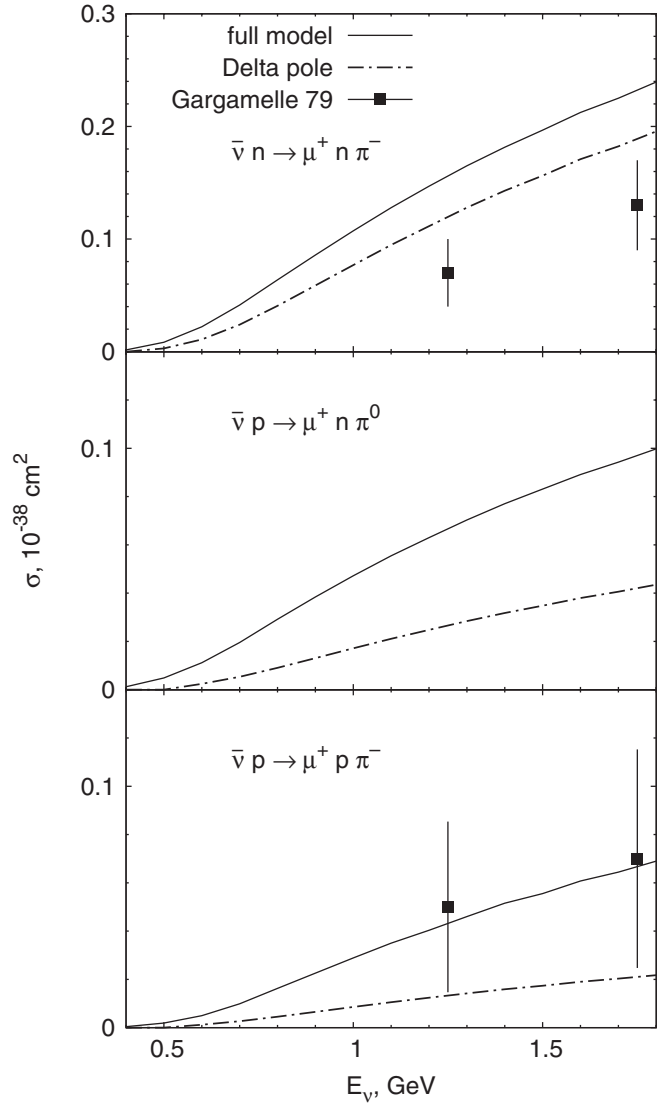


FIG. 6. The integrated one pion cross section, with kinematical cut $W(N\pi) < 1.4$ GeV versus the antineutrino energy for various final states.

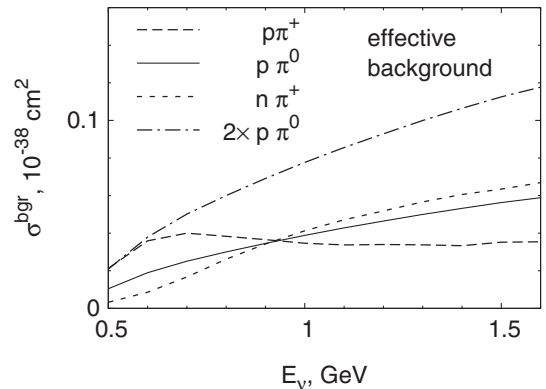


FIG. 7. The effective background versus the neutrino energy for various final states.

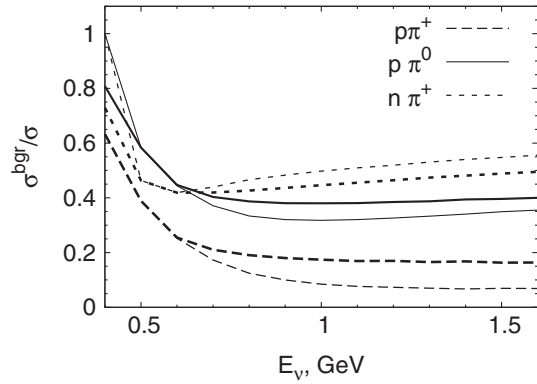


FIG. 8. The ratios of the effective background to the full model cross section versus the neutrino energy for various final states for the cuts $W(N\pi) < 1.4$ GeV (thin lines) and $W(N\pi) < 1.3$ GeV (thick lines).

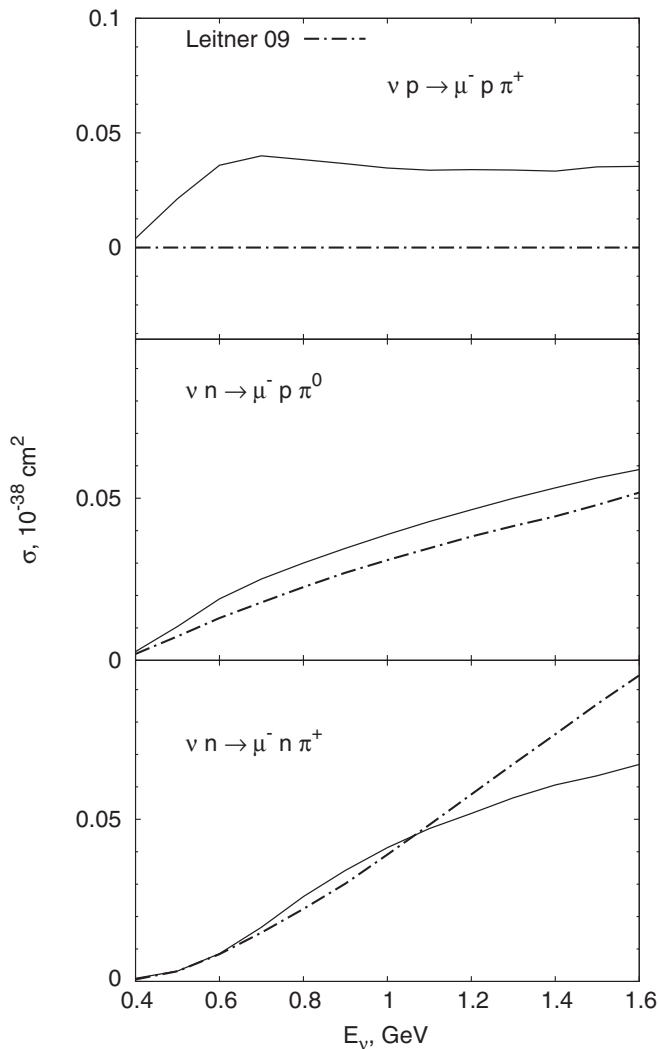


FIG. 9. The effective background versus the neutrino energy: comparison with the phenomenological calculations of [9].

others, the corresponding relation is different from $\sqrt{2}$, and interference also plays an important role.

Figure 8 shows the ratio of the background to the full model cross section. To investigate how sensitive this result is to the $W(N\pi)$ cut, we plot two curves for each final state: with the cut $W(N\pi) < 1.4$ GeV (thin lines) and $W(N\pi) < 1.3$ GeV (thick lines). As one can easily see, the results for these two cases are very close. For the $p\pi^+$ channel, the ratio is large for low energy, but steeply falls down and does not exceed 10% for $E_\nu > 1$ GeV. For the neutron target the background is large and is at the level of 35% for the $p\pi^+$ channel and 50% for $n\pi^+$ one.

Recall, that the background seen in neutrino reactions (weak background) include vector, axial and vector-axial-interference parts. In electron reactions, only the vector part is present (electromagnetic background) and well constrained by data. In [9] it was assumed, that $d\sigma_{\text{bgr}}^A$ and $d\sigma_{\text{bgr}}^{VA}$ have the same functional form as the vector part:

$$d\sigma_{\text{bgr}}^V + d\sigma_{\text{bgr}}^A + d\sigma_{\text{bgr}}^{VA} = (1 + b^{N\pi})d\sigma_{\text{bgr}}^V. \quad (18)$$

The vector parts were extracted from data independently for various channels. The coefficient b was the adjustable parameter fitted to the ANL data under the assumption $b^{n\pi^+} = 2b^{p\pi^0}$.

Figure 9 compares the effective background of the HNV model (solid lines) with the phenomenological background (18) (dash-dotted lines) for the three final states. The agreement between the curves is reasonable for all final states up to $E_\nu = 1.2$ GeV, which justifies the model used in [9].

VI. COMPARISON WITH THE ANL EXPERIMENT

As we already mentioned, the data on neutrino-nucleon interactions are scarce and come from the late 1970s and early 1980s. In all these experiments wide band neutrino beams were incident on hydrogen and/or deuterium targets. The most detailed sets of data are provided by the ANL 12-ft and the BNL 7-ft bubble chambers. The integrated cross sections from ANL and BNL experiments were already used in the previous section. However, valuable information comes also from the differential cross sections.

The deuteron effects for relevant neutrino energies were studied in [5], where three different wave functions, corresponding to the Hulthen, Bonn, and Paris NN models, were considered. It was shown, that these effects depend on the model used and generally suppress the cross section at $Q^2 < 0.1$ GeV² by no more than 8% for ANL experiment. At higher Q^2 they are practically negligible. For recent calculations including deuteron effects, see [11,34].

The GiBUU model implements the Argonne V18 NN potential. Within this model the deuteron effects are shown [20] to introduce only a minor correction to the ANL Q^2 distribution—the correction is even smaller for

BNL because of the higher neutrino energy. For invariant mass distributions, which are integrated over Q^2 , it would be even smaller. Thus, for the present calculations we neglect the effects of the deuteron structure.

A. Transformation from events to absolute cross section

Many reaction rates were presented in [2] not as absolute cross sections, but as events per some interval of the measured variable (Q^2 or W , for example). This is mainly explained by the fact, that neutrino fluxes are not precisely known, but can only be determined with some accuracy which is hard to estimate. For the ANL experiment, for example, the flux is calculated from the measured multiplication production cross section on a beryllium target and is given in [35]. It is clear, however, that the transformation coefficient k from the number of events per unit energy to the absolute cross section is unique for a given experiment and (for a perfect experiment) must be the same for each reaction channel $ch = (p\pi^+, p\pi^0, n\pi^+)$ for all distributions.

The ANL experiment provides data for the distribution of observed (also called raw) events $N_{ch}(E_\nu)$ in neutrino energy [2] (see Fig. 7 there),³ which is

$$f_{ch} \cdot N_{ch}(E_\nu) = \sigma_{\text{tot}(ch)}(E_\nu) \cdot \text{flux}(E_\nu) \cdot k. \quad (19)$$

The rate correction coefficients f_{ch} account for experimental backgrounds and losses. They can be extracted from the summary of rate corrections [2] (see Table I there) or calculated as ratios of corrected to raw events [2]:

$$\begin{aligned} f_{p\pi^+}^{\text{ANL}} &= \frac{1115}{871} = 1.280, & f_{p\pi^0}^{\text{ANL}} &= \frac{272.8}{202.2} = 1.349, \\ f_{n\pi^+}^{\text{ANL}} &= \frac{255.8}{206.2} = 1.241. \end{aligned} \quad (20)$$

With this data in hand and considering the flux and cross section as experimentally determined, we are able to calculate the coefficient k for different final states, compare the results and thus estimate the accuracy intrinsic to the experiment and its consistency.

Figure 10 shows the coefficients k determined from Eq. (19) and the ANL data. The flux is taken from the histogram in [35]. The experimental points for the cross sections are interpolated with splines. The errors for the cross sections are used to estimate the error bands of the coefficient.

For each channel, the middle curve shows the central value of k which corresponds to the central value of the cross section. The lower (upper) curves correspond to the maximal (minimal) values of the cross section and serve as error bands for k . For each channel k is fitted as a constant value, each point weighted with its maximal error.

³Note that neither ANL nor BNL provide distributions corrected for the experimental backgrounds, which, ideally, would be the subject of comparison with the theory.

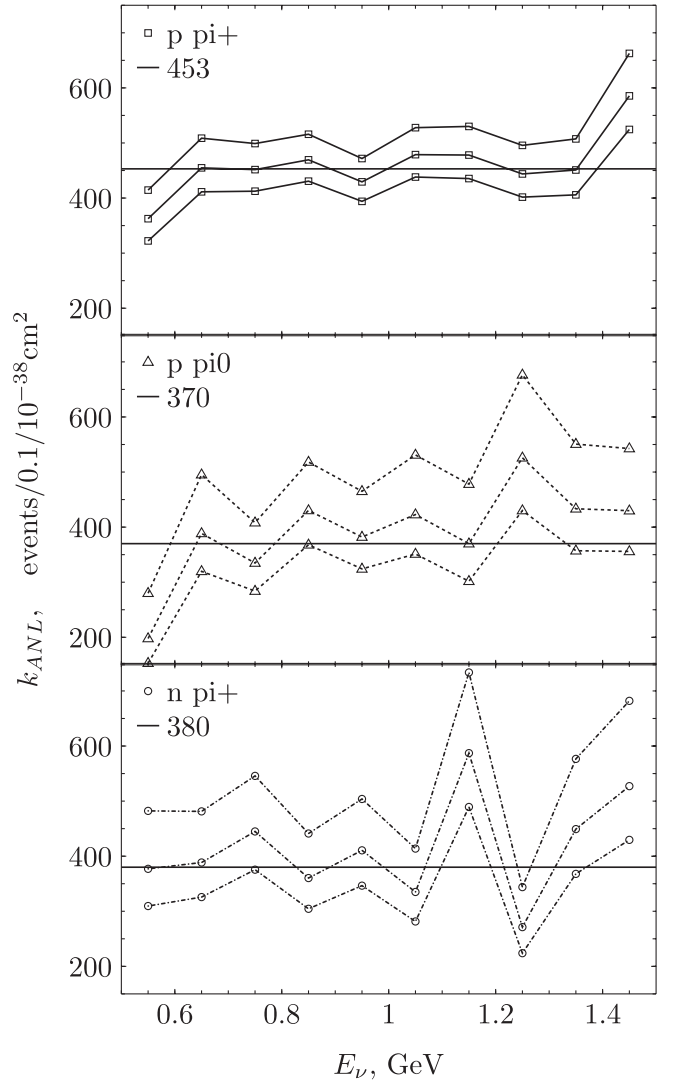


FIG. 10. The ANL transformation coefficient, determined from the data on neutrino event distributions for various final states. The three lines reflect an error band obtained from the errors of the published data.

The results

$$\begin{aligned} k_{\text{ANL}}^{p\pi^+} &= (453 \pm 16) \frac{\text{events}/0.1}{10^{-38} \text{ cm}^2}, \\ k_{\text{ANL}}^{p\pi^0} &= (370 \pm 31) \frac{\text{events}/0.1}{10^{-38} \text{ cm}^2}, \\ k_{\text{ANL}}^{n\pi^+} &= (380 \pm 31) \frac{\text{events}/0.1}{10^{-38} \text{ cm}^2} \end{aligned} \quad (21)$$

are shown as straight lines in Fig. 10. The factor 0.1 comes from the E_ν binning in Fig. 10.

Comparing k_{ANL} with the corresponding values for each channel separately, we conclude that an accuracy of around $(453 - 370) * 2 / (453 + 370) \approx 20\%$ should be attributed to it. This value is consistent with the ANL flux uncertainty estimated in [2] as 15%.

The procedure considered here is inverse to what experimentalists do to determine the absolute cross sections. Here its main purpose is to estimate a reasonable accuracy requirement for fitting theoretical curves to the data. We conclude, that for the ANL experiment an agreement within 20% should be considered as perfect.

B. Q^2 distribution

For the $p\pi^+$ channel the Q^2 distribution is given by the ANL experiment as an absolute cross section $d\sigma/dQ^2$ for events with the invariant nucleon-pion mass cut $W < 1.4$ GeV and neutrino energy cut 0.5 GeV $< E_\nu < 6$ GeV. Our results, presented in Fig. 11, show a good agreement with the experimental data.

The same distribution, but without energy cut, as well as those for the $p\pi^0$ and $n\pi^+$ channels, are presented as events per Q^2 interval. As mentioned before, the axial form factors of the theoretical model were fitted to the $p\pi^+$ channel of the ANL data; we thus use $k_{\text{ANL}} = k_{\text{ANL}}^{p\pi^+}$ given in Eq. (21) as our transformation coefficient for all distributions. In comparing our theoretical results with the data we therefore normalize them to each other by multiplying the theory results with the factor $k_{\text{ANL}}/f_{\text{ch}}$ with f_{ch} for the various channels given in Eq. (20).

Our results are shown in Fig. 12 and compared with the experimental histograms. The Delta pole contributions to the $p\pi^0$ and $n\pi^+$ channels are noticeably below the data. The extra contribution from the background adds around 50% for the $p\pi^0$ channel, which overshoots the data at low Q^2 . The general agreement of our curve with the data is very good. For the $n\pi^+$ channel, the background contribution adds 100% to the cross section, which, however, is still not enough to reach the experimentally observed values at low Q^2 . This could hint at a contribution of the higher mass isospin-1/2 resonances, not considered in this work, which may decay into one pion final state. With the estimated intrinsic uncertainty of 20%, the overall agreement should be considered as good.

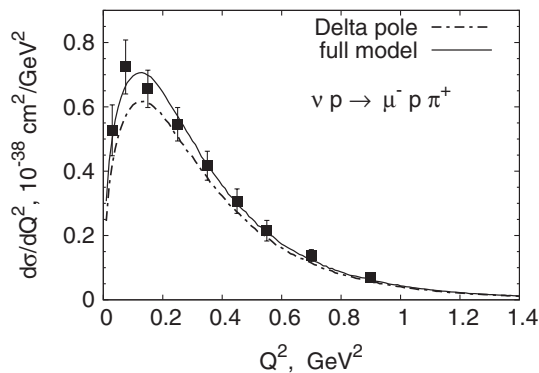


FIG. 11. Cross section $d\sigma/dQ^2$ averaged over the ANL neutrino energy flux for the final state $\mu^- p\pi^+$. The integration over W is performed with a $W < 1.4$ GeV cut, in agreement with the experiment [2]. Data are shown as filled squares.

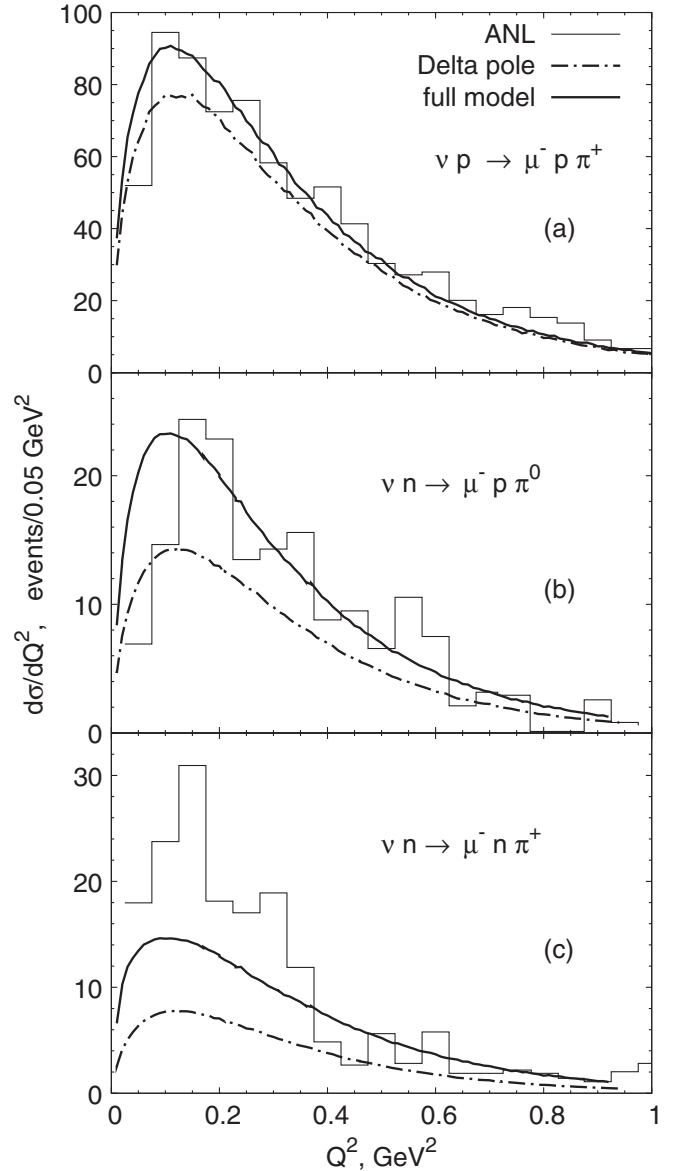


FIG. 12. Cross section $d\sigma/dQ^2$ averaged over the ANL neutrino energy flux for the final states: (a) $\mu^- p\pi^+$, (b) $\mu^- p\pi^0$, and (c) $\mu^- n\pi^+$. The integration over W is performed with a $W < 1.4$ GeV cut, in agreement with the experiment [2]. Data are shown as histograms.

C. W distributions

Next, we present data for invariant mass distributions. In previous theoretical investigations [4,6,14], only distributions versus pion-nucleon invariant mass $W(N\pi)$ were calculated. The ANL and BNL experimental data are available also for nucleon-muon $W(\mu N)$ and pion-muon $W(\mu\pi)$ combinations. These additional data can be used to constrain the theory even further.

Figure 13(a) shows the $W(N\pi)$ distribution for the $p\pi^+$ channel. The agreement of our full model calculations (solid curve) with the histogram is very good. Of interest is the region of low W , near the one pion production

threshold. In this region, the experimental data show a noticeable rise with increasing W , which is in agreement with the full model prediction. The Delta pole contribution (dash-dotted curve), on the other hand, grows rather slowly.

For the $p\pi^0$ and $n\pi^+$ final states, as shown in Figs. 13(b) and 13(c) the agreement of the full model with the histogram is reasonable. For the $p\pi^0$ channel the full model overestimates events in the Delta peak region and underestimates them immediately above this peak. For the $n\pi^+$ channel, the data are underestimated below the Delta peak.

At low W the background gives a noticeable contribution for both channels, in line with the data. For different final states the background contributions above the Delta

peak are very different: small negative for $p\pi^+$, very small for $p\pi^0$ and positive for $n\pi^+$.

While the $W(N\pi)$ distributions are mainly sensitive to the Δ excitation, the distributions $W(\mu N)$ and $W(\mu\pi)$ test the angular distribution of the νN interaction.

The $W(\mu N)$ and $W(\mu\pi)$ distributions shown in Figs. 14 and 15 also agree reasonably well with our calculations. Recall, that in the ANL experiment the $p\pi^+$ data are presented for the whole neutrino energy flux, which only vanishes at $E_\nu = 6$ GeV. This can explain the large tail in this distribution. For the $p\pi^0$ and $n\pi^+$ final states, on the other hand, the experimental data (as well as our calculations) are limited to $E_\nu < 1.5$ GeV, so that the large $W(\mu N)$ are not kinematically accessible.

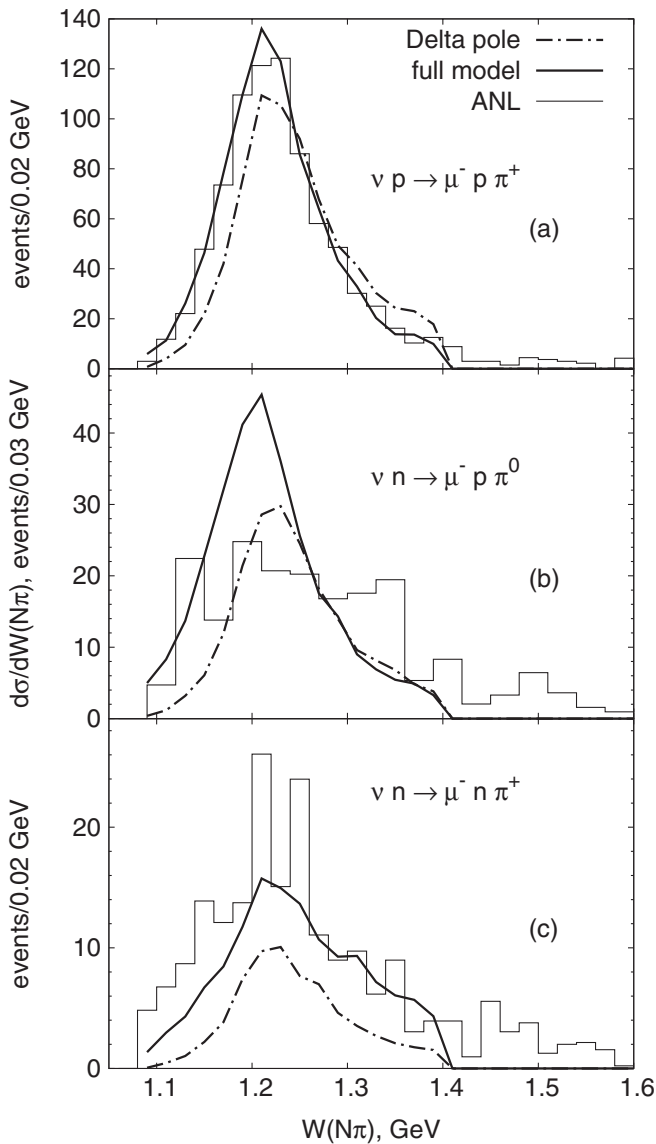


FIG. 13. The nucleon-pion invariant mass distributions, averaged over the ANL flux. The full model calculations (solid curve) and Delta pole contribution (dash-dotted curve) are shown. The experimental data from [2] are shown as histograms.

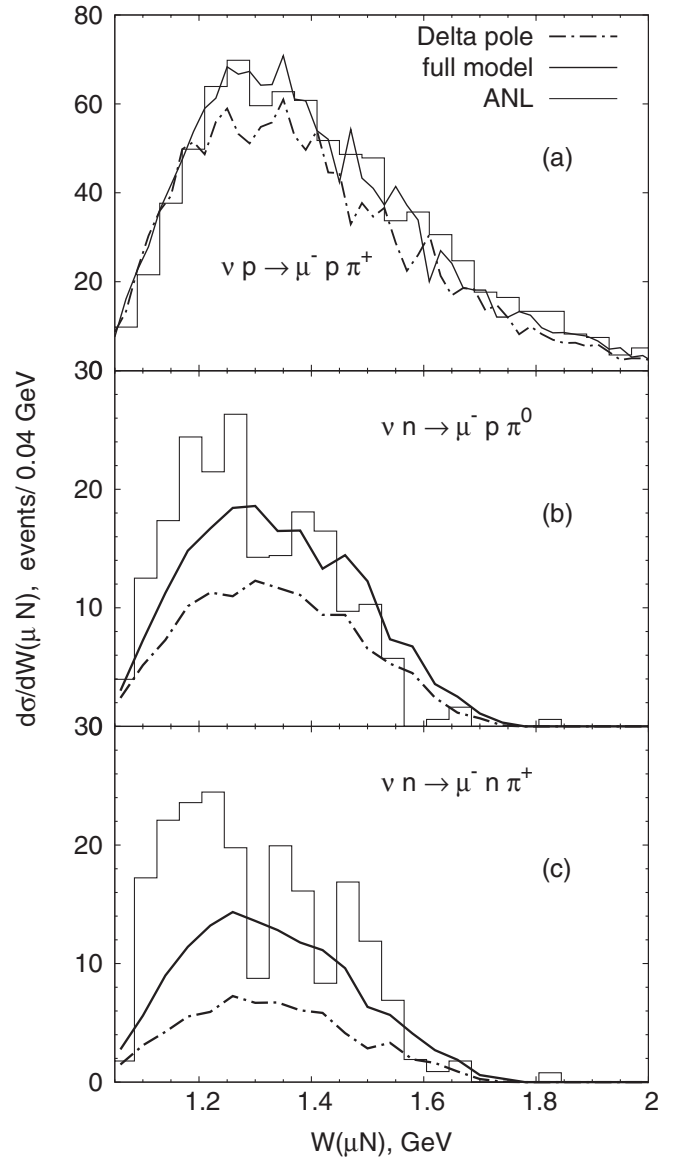


FIG. 14. The muon-nucleon invariant mass distributions, averaged over the ANL flux. The full model calculations (solid curve) and Delta pole contribution (dash-dotted curve) are shown. The experimental data from [2] are shown as histograms.

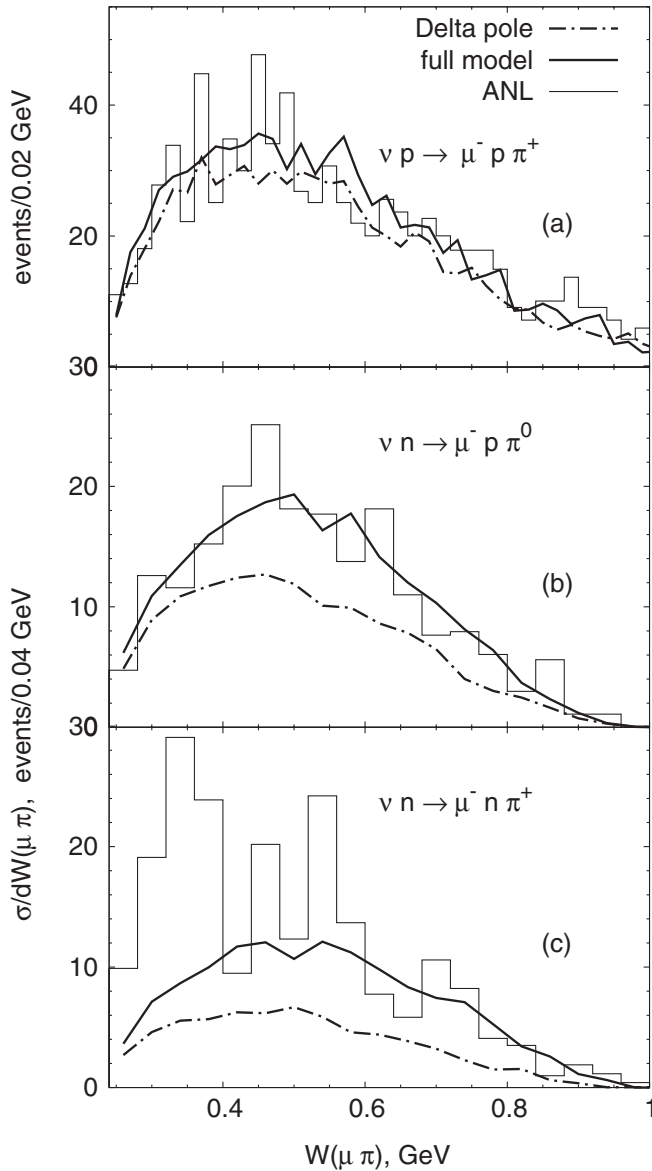


FIG. 15. The muon-pion invariant mass distributions, averaged over the ANL flux. The full model calculations (solid curve) and Delta pole contribution (dash-dotted curve) are shown. The experimental data from [2] are shown as histograms.

The full model and the Delta pole terms give curves of similar form, but different magnitude in the various isospin channels. For the $p\pi^+$ channel, the agreement of our full model with the data is very good. In the $p\pi^0$ channel the data are underestimated at low $W(\mu N)$. For the $n\pi^+$ channel, the data are underestimated at both low $W(\mu N)$ and low $W(\mu\pi)$.

The overall results clearly indicate the necessity to include the nonresonant contribution in addition to that of the Delta pole. Even with some underestimation, the full model curves show much better agreement with the whole set of data than the Delta pole terms alone. The background adds around 10% to the Dp cross section for the $p\pi^+$

channel, around 50% for the $p\pi^0$ one and around 100% for the $n\pi^+$ one.

From Figs. 13–15 we conclude, that within the experimental accuracy available, the data presented can discriminate between the Delta pole and the full model curves and are compatible with the HNV background model.

VII. COMPARISON WITH THE BNL EXPERIMENT

A. Transformation from events to absolute cross section

The results of the BNL experiment on Q^2 or W distributions, like those of the ANL experiment, are presented as events. Data on the distribution of events in neutrino energy are also available [3] (see Fig. 2 there), so we use the same procedure as before to determine the transformation coefficient and estimate its accuracy.

The rate correction coefficients f_{ch} for BNL are given in [3] (see Table II there)

$$f_{p\pi^+}^{\text{BNL}} = 1.12, \quad f_{p\pi^0}^{\text{BNL}} = 1.05, \quad f_{n\pi^+}^{\text{BNL}} = 0.89. \quad (22)$$

Figure 16 shows the coefficient k determined from Eq. (19) and the BNL data. The flux is calculated from the observed quasielastic events and given in [36]. The experimental points for the cross sections are interpolated with splines. The error bars of the cross sections are used to estimate the error bands of the coefficient.

For each channel, the middle curve with data points on it shows the central value of k , while the lower (upper) curves serve as error bands for k . For each channel, k is fitted as a constant value, each point weighted with its maximal error. The results

$$\begin{aligned} k_{\text{BNL}}^{p\pi^+} &= (518 \pm 29) \frac{\text{events}/0.2}{10^{-38} \text{ cm}^2}, \\ k_{\text{BNL}}^{p\pi^0} &= (528 \pm 30) \frac{\text{events}/0.2}{10^{-38} \text{ cm}^2}, \\ k_{\text{BNL}}^{n\pi^+} &= (544 \pm 42) \frac{\text{events}/0.2}{10^{-38} \text{ cm}^2} \end{aligned} \quad (23)$$

are shown as straight lines in Fig. 16.

Comparing k_{BNL} for the three channels, we attribute an accuracy of around $(544 - 518) * 2 / (544 + 518) = 5\%$ to k_{BNL} . We conclude, that when comparing with the BNL experiment, an agreement within 5% should be considered as perfect.

B. Q^2 distribution

The data on the Q^2 distribution for the $p\pi^+$ channel are presented in [3] for the neutrino energy cut $0.5 \text{ GeV} < E_\nu < 6 \text{ GeV}$ and the invariant mass cut $W < 1.4 \text{ GeV}$. Since the latter corresponds to the range of applicability of the HNV model, we can normalize the area under the full model theoretical curve to that under the experimental data. This is another way to estimate

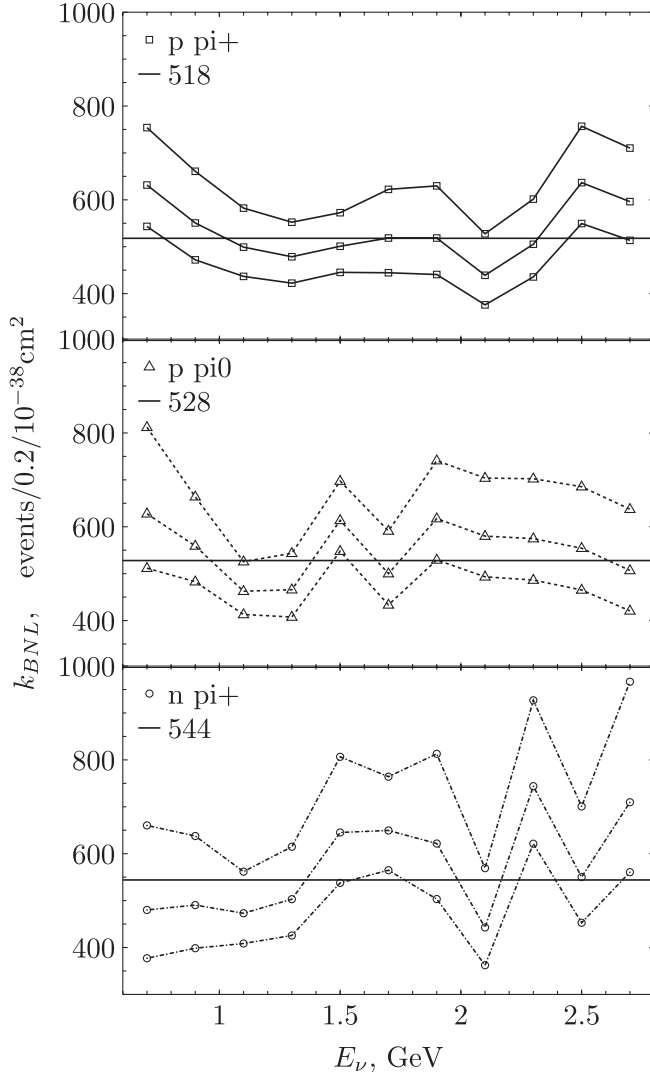


FIG. 16. The BNL transformation coefficient, determined from the data on neutrino event distributions for various final states. The three lines reflect an error band obtained from the errors of the published data.

the transformation coefficient $k_{\text{BNL}}^{Q^2}$ [which for a perfect experiment must be equal to those in Eq. (23)]:

$$\left(\frac{d\sigma}{dQ^2}\right)_{\text{exper}} = k_{\text{BNL}} \cdot \left(\frac{d\sigma}{dQ^2}\right)_{\text{theor}},$$

$$k_{\text{BNL}}^{Q^2} = 182.5 \frac{\text{events}/0.05 \text{ GeV}^2}{10^{-38} \text{ cm}^2/\text{GeV}^2} = 730 \frac{\text{events}/0.2}{10^{-38} \text{ cm}^2}. \quad (24)$$

This value exceeds the typical value of k_{BNL} determined in Eq. (23) by more than 30% (even more for the $p\pi^+$ channel), and thus cannot be considered as consistent.

Speculating about the possible origin of this inconsistency, we note that the values (23) for different channels agree among themselves quite well, which may hint at the consistent treatment of the rate correction coefficients f_{ch} .

Keeping also in mind, that the flux is the same for various channels, a possible way to explain the above inconsistency would be to suppose that the cross sections are overestimated by 30%. This is exactly the difference between ANL and BNL integrated cross sections. Thus, by reducing $\sigma_{\text{tot(ch)}}^{\text{BNL}}$ by 30% one would simultaneously reach agreement with ANL and obtain $k_{\text{BNL}}^{\text{ch}}$ consistent with $k_{\text{BNL}}^{Q^2}$.

With the data as they are, we reestimate a realistic uncertainty as 30%.

Thus, for the BNL experiment we aim at shape-only comparison and hereinafter use $k_{\text{BNL}}^{Q^2}$ (24) as our transformation coefficient.

The comparison of the Q^2 distribution with our calculations is shown in Fig. 17. For the $p\pi^+$ channel, as expected, the background gives only a small contribution in addition to the leading Delta pole term. In agreement with earlier calculations [32], the peak of the curve is located in the region $Q^2 = 0.1-0.12 \text{ GeV}^2$ and is shifted with respect to the data peak at $Q^2 = 0.18 - 0.2 \text{ GeV}^2$. This disagreement has been known for a long time with similar results obtained within various models [3,20,32,37] and is not resolved. Inclusion of the background does not change the peak position.

The data for the other channels are given in [3] without any cut on W , and for the whole neutrino flux (that is $0.34 \text{ GeV} < E_\nu < 6 \text{ GeV}$) as events per 0.1 GeV^2 interval. They are compared with our calculations in Fig. 18, where the same transformation coefficient $k_{\text{BNL}}^{Q^2}/f_{\text{ch}}^{\text{BNL}}$ [Eq. (24)] is used. The same coefficient is also used further for various W distributions.

For the $p\pi^+$ channel, as expected, our full model calculations (solid line) is below the experimental histogram. The area under our curve is 15% below the area under the histogram. Since the data include higher invariant masses whereas our calculations contain a cutoff of 1.4 GeV , corresponding to the range of validity of the HNV model,

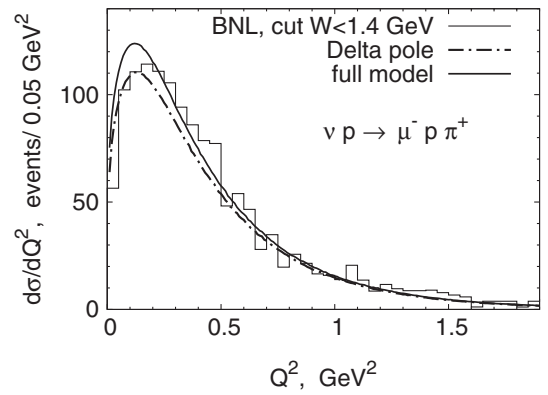


FIG. 17. Cross section $d\sigma/dQ^2$ averaged over the BNL neutrino energy flux for the final state $\mu^- p \pi^+$. The integration is performed with the $W(N\pi) < 1.4 \text{ GeV}$ cut, in agreement with the experimental data [3], which are shown as histogram.

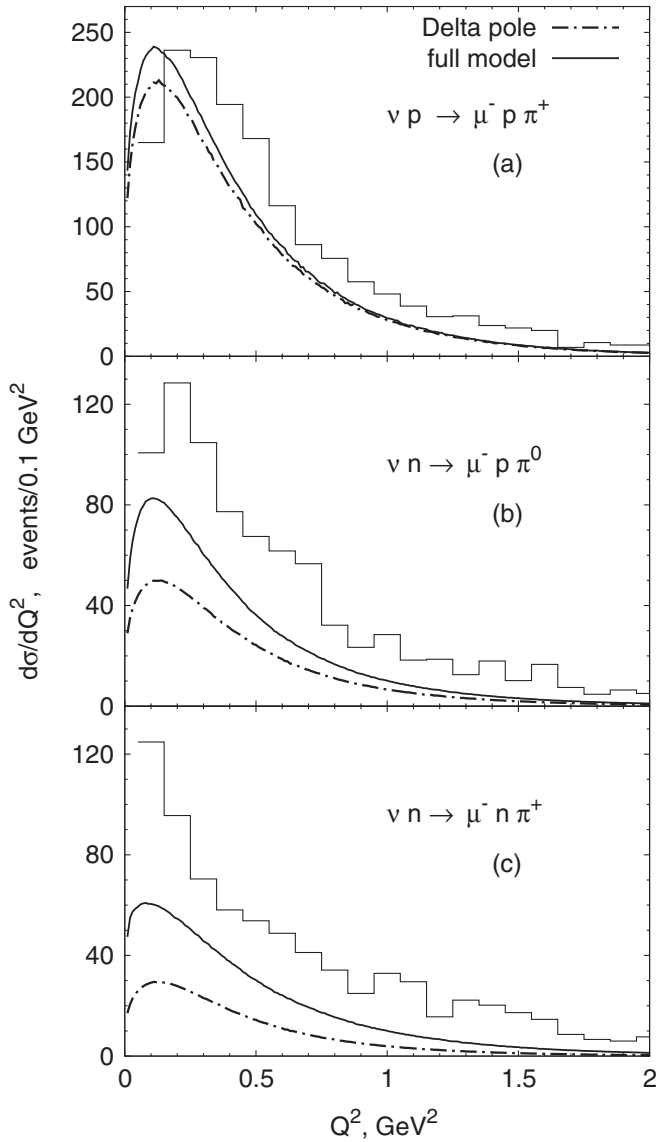


FIG. 18. The $d\sigma/dQ^2$ cross section averaged over the BNL neutrino energy flux for the final states: (a) $\mu^- p \pi^+$, (b) $\mu^- p \pi^0$, and (c) $\mu^- n \pi^+$. The integration is performed with the $W(N\pi) < 1.4$ GeV cut, corresponding to the range of applicability of the HNV model. The experimental data [3] shown as histograms are without W cut.

this implies that 15% of all events in this channel should be attributed to the higher mass isospin-3/2 resonances, such as $P_{33}(1600)$, $S_{31}(1620)$, $D_{33}(1700)$, and their interferences with the background, which are not considered here.

For the $p\pi^0$ and $n\pi^+$ channel, the background significantly increases the cross section in comparison with the Delta pole contribution. However, our full model curves are still much lower than the histograms, which indicates a large contribution of higher mass isospin-1/2 and -3/2 resonances and their interferences. The relative importance of these events is estimated by comparing the areas under the theoretical curve and experimental histogram, as it was

described for the $p\pi^+$ channel, and it appears to be 43% for $p\pi^0$ and 46% for $n\pi^+$. This will also be demonstrated further in the $W(N\pi)$ invariant mass distribution.

Notice also, that in the $p\pi^0$ channel [Fig. 18(b)] the peak of our curve is shifted to the left with respect to the histogram. This effect is the same as in $p\pi^+$ channel in Fig. 17, but it is revealed here with less significance because of the larger Q^2 binning.

C. W distribution

Now we proceed with calculating the invariant mass distributions. Figure 19 shows the $W(N\pi)$ distribution for

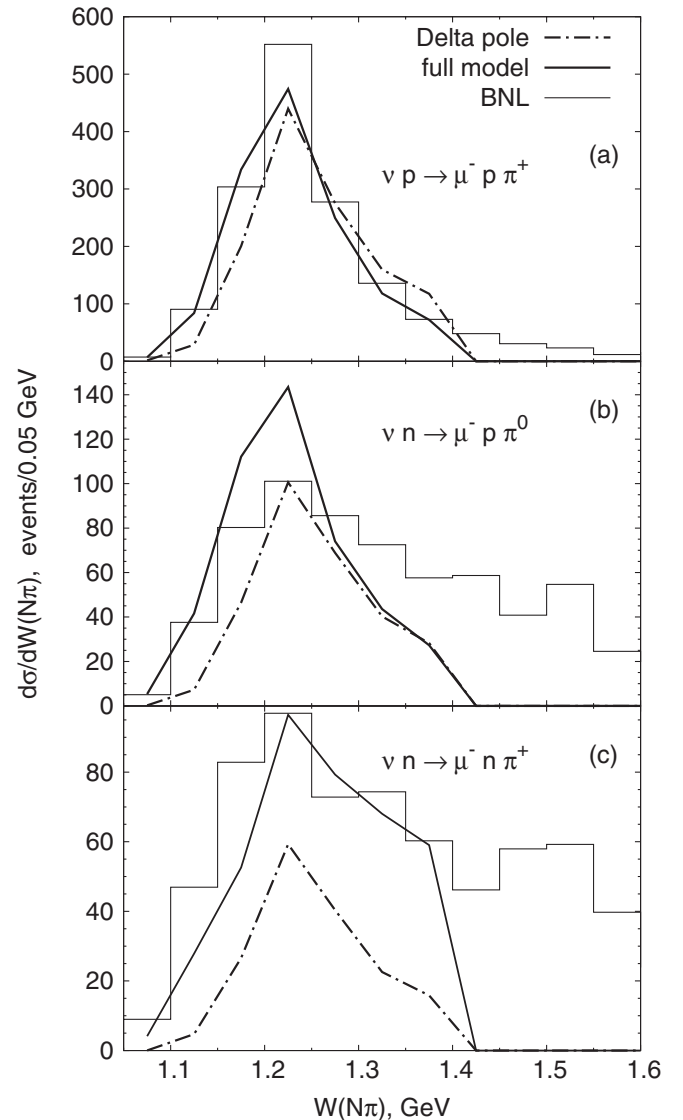


FIG. 19. The nucleon-pion invariant mass distributions, averaged over the BNL flux. The full model calculations (solid curve) and Delta pole contribution (dash-dotted curve) are shown with the cut $W(N\pi) < 1.4$ GeV. The experimental BNL data [3] which do not contain this cut are shown as histograms.

the three final states. Our calculations are done only up to $W < 1.4$ GeV, which is the range of applicability of the HNV model, while the experimental data are available also for higher W .

For the $p\pi^+$ channel, our calculations show a very good agreement with the data. In the region 1.05 GeV $< W < 1.4$ GeV the area under our curve coincides with the area under the histogram with an accuracy better than 1%.

To estimate how many events belong to the high $W(N\pi)$ region, we calculate the area under the histogram with the cut $W(N\pi) < 2.0$ GeV and compare it to that with the cut $W(N\pi) < 1.4$ GeV. We find that $\geq 10\%$ of all events belong to the $W(N\pi) > 1.4$ GeV region. This is in agreement with the conclusion previously derived from the Q^2 distributions.

For both the $p\pi^0$ and $n\pi^+$ channels, the background is essential, especially at very low $W(N\pi)$, where it significantly increases the cross sections. The overall agreement of our calculations with the data is reasonable. Similar to our comparison with the ANL experiment, for the $p\pi^0$ channel the full model overestimates the data in the region of Delta peak and underestimates them immediately above this peak. For the $n\pi^+$ channel, the data are underestimated below the Delta peak. The percentage of events with $W(N\pi) > 1.4$ GeV is estimated to be 45% for the $p\pi^0$ and 44% for the $n\pi^+$, which is in good agreement with the previous results obtained when discussing the Q^2 distribution.

As in our calculations for the ANL experiment, in the W region above the Delta peak the background contribution is different for different channels: negative for $p\pi^+$, small for $p\pi^0$ and positive for $n\pi^+$. The comparison of the two latter channels shows that the effective background $d\sigma^{\text{bgr}}/dW(N\pi)$ as it is described within the HNV model does not support the isospin-1/2 hypothesis.

Figure 20 shows the muon-nucleon invariant mass distribution compared with the BNL data subject to selection $W(N\pi) < 1.4$ GeV.

For the $p\pi^+$ channel, the background slightly increases the cross section. For the $p\pi^0$ and $n\pi^+$ channels it gives a significant contribution, which noticeably improves agreement with the histograms. For the $p\pi^0$ channel, the data show an excess of events over our curve at low $W(\mu N)$. As explained in [3], "this excess comes in part from the misidentified $\nu n \rightarrow \nu\pi^- p$ and $nn \rightarrow n p\pi^-$ events which belong to the experimental background" not subtracted from the data.

This generally means that the experimental background is nonuniform and requires a more detailed treatment. Indeed, all experimental histograms show the distributions of observed (raw) events. The rate correction factors $f_{\text{ch}}^{\text{BNL}}$ are provided experimentally as constant factors that do not depend on kinematics. In this way, we correct the total number of events, but the nonuniformity

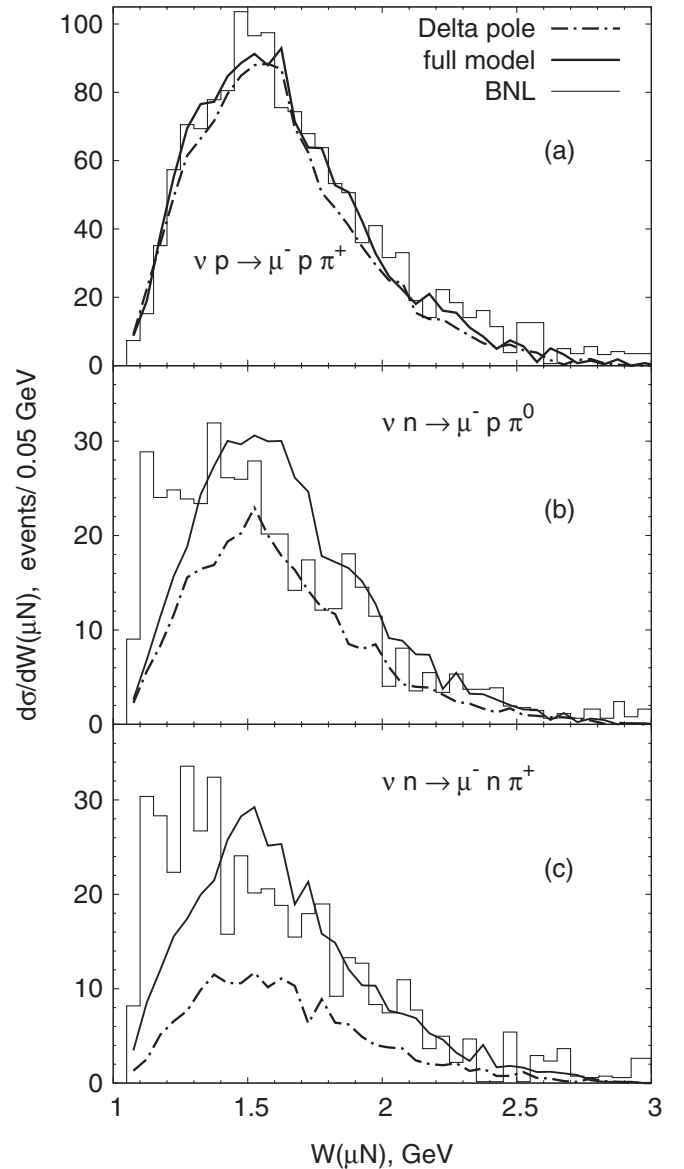


FIG. 20. The muon-nucleon invariant mass distributions, averaged over the BNL flux, for the events with $W(N\pi) < 1.4$ GeV compared to the BNL data [3] shown as histograms.

of the experimental corrections remains unaccounted for and can reveal itself in all distributions.

For the $n\pi^+$ channel, the agreement is good in the region of high $W(\mu N)$, but again we underestimate the data for low $W(\mu N)$.

Figure 21 shows the muon-pion invariant mass distribution compared with the BNL data subject to selection $W(N\pi) < 1.4$ GeV. The agreement of our calculations with the data is good for the $p\pi^+$ and $p\pi^0$ channels, while for the $n\pi^+$ one we underestimate the data at low $W(\mu\pi)$.

All the three W distributions taken together clearly show the importance of background terms in reaching a reasonable description of the data for all the three invariant mass

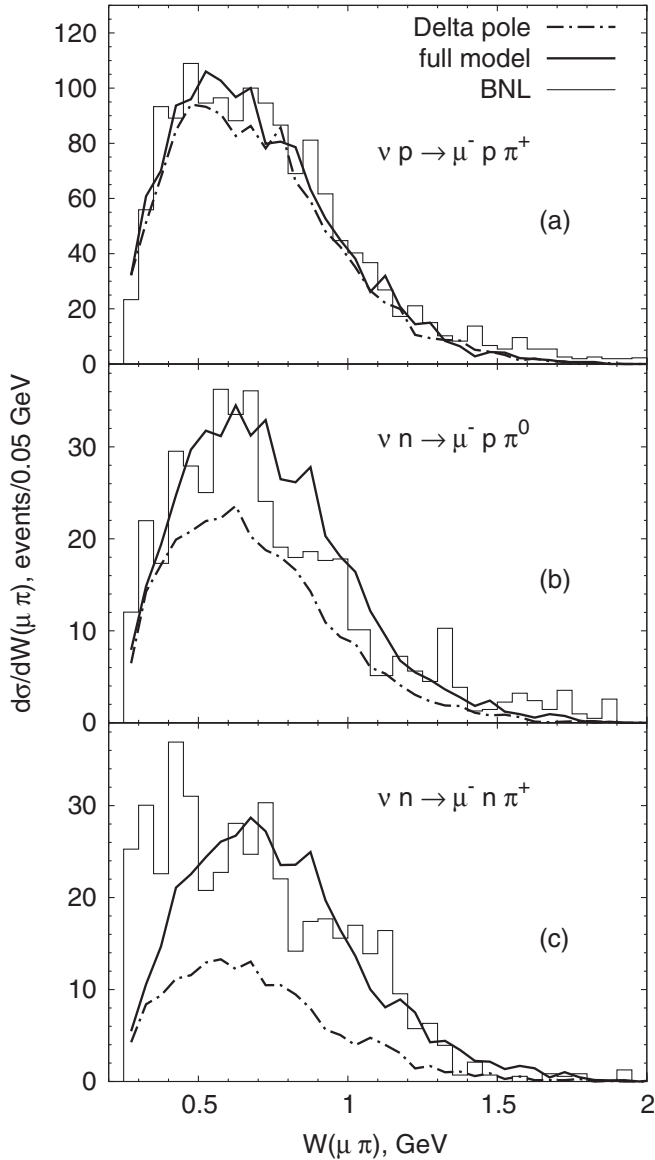


FIG. 21. The muon-pion invariant mass distributions, averaged over the BNL flux, for the events with $W(N\pi) < 1.4$ GeV compared to the BNL data [3] shown as histograms.

distributions considered. Delta pole term alone, showing a good agreement with the data for the $p\pi^+$ channel, significantly underestimates all the data for the $p\pi^0$ and $n\pi^+$ channels.

Some discrepancies between the full model calculations and data at low W s [for all three $W(N\pi)$, $W(\mu N)$ and $W(\mu\pi)$] for both ANL and BNL may point to the necessity to improve the model. As discussed earlier in this section, the BNL experimentalists themselves attributed the excess of events in $W(\mu N)$ distribution of the $p\pi^0$ channel to some misidentified events. Similar excess in other channels for low W may have a similar origin.

VIII. DISCUSSION AND CONCLUSION

In Sec. II we have outlined the HNV model and the phenomenological form factors for various diagrams. As ensured by comparison with electroproduction in Sec. III the model is applicable up to nucleon-pion invariant mass of $W(N\pi) < 1.4$ GeV and provides about the same level of accuracy as the MAID model.

For neutrino reactions, as discussed in Sec. IV, the model predicts a background contribution, which is small for the $p\pi^+$ channel (at the level below 10% for neutrino energies above 1 GeV), at the level of 30% (with respect to the full model cross section, that is 50% with respect to the Delta pole contribution) for the $p\pi^0$ channel and at the level of 50% (with respect to the full model cross section, that is 100% with respect to the Delta pole contribution) for the $n\pi^+$ channel. The effective background does not satisfy the isospin-1/2 hypothesis.

The HNV model describes the available data set on neutrino and antineutrino reactions on nucleons reasonably well, with an accuracy that approximately corresponds to the accuracy with which different data agree among themselves.

For neutrinos the absolute values of the integrated cross section are available from the ANL and BNL experiment, with the BNL data being systematically higher. The Delta axial form factors were fitted in [14] to the ANL integrated cross section and the Q^2 distribution for the $p\pi^+$ channel so that the full model agrees with them by definition. Agreement with the ANL data for the $p\pi^0$ and $n\pi^+$ channels shows that the model gives a good description of the background. The BNL data lie around 30% higher for all channels.

For antineutrinos only very few data are available from the Gargamelle experiments. The agreement of the full model calculations with the data is good for the $p\pi^-$ channel and overestimates the data for the $n\pi^-$ one.

For most of the differential cross sections available experimentally no information about the absolute value of the cross section is available; the data are presented as raw events per Q^2 or W interval. By estimating the transformation coefficients for the ANL and BNL experiments in Secs. VIA and VIIA, we have shown that the realistic accuracy for the ANL experiment is around 20%, with the uncertainties coming from the inconsistencies in the various channels. For the BNL experiment, the various channels agree within 5%; here the overall accuracy about 30% comes from the disagreement of the Q^2 distribution, discussed in Sec. VII B, with the integrated event distribution.

As discussed in Secs. VI and VII, the overall agreement with the data is perfect for the $p\pi^+$ channel and reasonable for the $p\pi^0$ and $n\pi^+$ ones. For the latter two channels, the full model calculations systematically underestimate the experimental histograms at low W s. These discrepancies may hint at the necessity to improve the model, but they

may as well come from the recognized nonuniformity of the experimental background.

Even without absolute normalization, and even taking into account the discrepancies observed, all the ANL and BNL data taken together are able to discriminate between the full model and the leading Delta pole contribution. When all three final states accessible for neutrino reactions ($p\pi^+$, $p\pi^0$, $n\pi^+$) are considered, the data definitely

demand the nonresonant background and favor the full model calculations.

ACKNOWLEDGMENTS

This work is supported by DFG. The authors are grateful to M. Valverde for providing us with his unpublished results for comparison.

-
- [1] V.D. Burkert and T. S. H. Lee, *Int. J. Mod. Phys. E* **13**, 1035 (2004).
 - [2] G. M. Radecky *et al.*, *Phys. Rev. D* **25**, 1161 (1982).
 - [3] T. Kitagaki *et al.*, *Phys. Rev. D* **34**, 2554 (1986).
 - [4] D. Rein and L. M. Sehgal, *Ann. Phys. (N.Y.)* **133**, 79 (1981).
 - [5] L. Alvarez-Ruso, S. K. Singh, and M. J. Vicente Vacas, *Phys. Rev. C* **59**, 3386 (1999).
 - [6] E. A. Paschos, J.-Y. Yu, and M. Sakuda, *Phys. Rev. D* **69**, 014013 (2004).
 - [7] O. Lalakulich, E. A. Paschos, and G. Piranishvili, *Phys. Rev. D* **74**, 014009 (2006).
 - [8] E. Hernandez, J. Nieves, S. K. Singh, M. Valverde, and M. J. Vicente Vacas, *Phys. Rev. D* **77**, 053009 (2008).
 - [9] T. Leitner, O. Buss, L. Alvarez-Ruso, and U. Mosel, *Phys. Rev. C* **79**, 034601 (2009).
 - [10] K. M. Graczyk and J. T. Sobczyk, *Phys. Rev. D* **77**, 053001 (2008).
 - [11] E. Hernandez, J. Nieves, M. Valverde, and M. J. Vicente Vacas, *Phys. Rev. D* **81**, 085046 (2010).
 - [12] D. Drechsel, S. S. Kamalov, and L. Tiator, *Eur. Phys. J. A* **34**, 69 (2007).
 - [13] T. Sato, D. Uno, and T. S. H. Lee, *Phys. Rev. C* **67**, 065201 (2003).
 - [14] E. Hernandez, J. Nieves, and M. Valverde, *Phys. Rev. D* **76**, 033005 (2007).
 - [15] C. Barbero, G. Lopez Castro, and A. Mariano, *Phys. Lett. B* **664**, 70 (2008).
 - [16] For details, see GIBUU, <http://gibuu.physik.uni-giessen.de/GiBUU>.
 - [17] T. Leitner, L. Alvarez-Ruso, and U. Mosel, *Phys. Rev. C* **73**, 065502 (2006).
 - [18] T. Leitner, L. Alvarez-Ruso, and U. Mosel, *Phys. Rev. C* **74**, 065502 (2006).
 - [19] T. Leitner, O. Buss, U. Mosel, and L. Alvarez-Ruso, *Phys. Rev. C* **79**, 038501 (2009).
 - [20] T. J. Leitner, Ph.D. thesis, Giessen University, Germany, 2009.
 - [21] S. Ahmad, M. Sajjad Athar, and S. K. Singh, *Phys. Rev. D* **74**, 073008 (2006).
 - [22] C. Praet, O. Lalakulich, N. Jachowicz, and J. Ryckebusch, *Phys. Rev. C* **79**, 044603 (2009).
 - [23] A. Gil, J. Nieves, and E. Oset, *Nucl. Phys. A* **627**, 543 (1997).
 - [24] G. E. Hite, R. J. Jacob, and M. D. Scadron, *Phys. Rev. D* **14**, 1306 (1976).
 - [25] Y. Kitazawa, *Phys. Lett.* **151B**, 165 (1985).
 - [26] S. Narison, *Phys. Lett. B* **216**, 191 (1989).
 - [27] A. Bodek, S. Avvakumov, R. Bradford, and H. S. Budd, *J. Phys. Conf. Ser.* **110**, 082004 (2008).
 - [28] K. S. Kuzmin, V. V. Lyubushkin, and V. A. Naumov, *Eur. Phys. J. C* **54**, 517 (2008).
 - [29] M. E. Christy and P. E. Bosted, *Phys. Rev. C* **81**, 055213 (2010).
 - [30] S. Galster *et al.*, *Phys. Rev. D* **5**, 519 (1972).
 - [31] D. Drechsel, O. Hanstein, S. S. Kamalov, and L. Tiator, *Nucl. Phys. A* **645**, 145 (1999).
 - [32] O. Lalakulich and E. A. Paschos, *Phys. Rev. D* **71**, 074003 (2005).
 - [33] T. Bolognese, J. P. Engel, J. L. Guyonnet, and J. L. Riester, *Phys. Lett.* **81B**, 393 (1979).
 - [34] K. M. Graczyk, D. Kielczewska, P. Przewlocki, and J. T. Sobczyk, *Phys. Rev. D* **80**, 093001 (2009).
 - [35] S. J. Barish *et al.*, *Phys. Rev. D* **16**, 3103 (1977).
 - [36] N. J. Baker *et al.*, *Phys. Rev. D* **23**, 2499 (1981).
 - [37] K. M. Graczyk and J. T. Sobczyk, *Phys. Rev. D* **77**, 053003 (2008).